Nanoscale

PAPER

View Article Online
View Journal | View Issue

Cite this: *Nanoscale*, 2023, **15**, 7384

Polypropylene sulphide coating on magnetic nanoparticles as a novel platform for excellent biocompatible, stimuli-responsive smart magnetic nanocarriers for cancer therapeutics†

Meenakshi Chauhan,‡ Suparna Mercy Basu,‡ Mohd Qasim and Jyotsnendu Giri *

Magnetic nanoparticle (MNP) delivery systems are promising for targeted drug delivery, imaging, and chemo-hyperthermia of cancer; however, their uses remain limited primarily due to their toxicity associated with reactive oxygen species (ROS) generation, targeted delivery, and biodegradation. Attempts employing polymer coatings to minimize the toxicity, along with other challenges, have had limited success. We designed a novel yet generic 'one-for-all' polypropylene sulphide (PPS) coated magnetic nano-delivery system (80 ± 15 nm) as a multi-faceted approach for significant biocompatibility improvement, loading of multiple drugs, ROS-responsive delivery, and combined chemo-hyperthermia therapy for biomedical applications. Three distinct MNP systems (15 ± 1 nm) were fabricated, coated with PPS polymer, and investigated to validate our hypothesis and design. Simultaneous degradation of MNPs and PPS coatings with ROS-scavenging characteristics boosted the biocompatibility of MNPs 2–3 times towards non-cancerous fibroblasts (NIH3T3) and human epithelial cells (HEK293). In an alternating magnetic field, PPS-MNPs (MnFe) had the strongest heating characteristics (SAR value of 240 W g^{-1}). PPS-MNP drug-loaded NPs were efficiently internalised into cells and released 80% of the drugs under tumor microenvironment-mimicking (pH 5–7, ROS) conditions, and demonstrated effective chemo-hyperthermia (45 °C) application for breast cancer cells with 95% cell death in combined treatment *vs.* 55% and 30% cell death in only hyperthermia and chemotherapy respectively.

Received 21st September 2022,
Accepted 14th January 2023

DOI: 10.1039/d2nr05218k

rsc.li/nanoscale

1. Introduction

Magnetic nanoparticles (MNPs) have become promising nanomaterials in the biomedical field. MNPs, especially superparamagnetic nanoparticles, have been extensively explored in various research areas, including targeted drug delivery, magnetic resonance imaging (MRI), regenerative medicine, tissue repair, cell tracking, cell sorting, biosensing, magnetic field-assisted radionuclide therapy and hyperthermia for cancer treatment.[1–4] In recent years, the US-FDA has approved different formulations of MNPs for various applications, such as Feridex® (ferumoxides),[5] imaging contrast agents for the detection of liver lesions, and Feraheme® (ferumoxytol)[6] for anemic iron deficiency treatment in adult patients. Similarly, several substituted ferrites such as $MnFe_2O_4$ (MnFe), $CoFe_2O_4$ (CoFe), $NiFe_2O_4$ (NiFe) have been reported for their unique magnetic properties, enhanced MRI contrast ability and heating properties for their most promising biomedical applications.[7] However, the vast uses of these MNPs are still limited due to their high toxicity associated with these multivalent transition metal ions (Fe, Mn, Co, Ni)[8–10] and their degradation and toxicity in the human body. Among the different physicochemical properties of MNPs contributing to their toxicity, the presence of metal ions and their propensity to form reactive oxygen species (ROS) are regarded the most important factors in the toxicity of MNPs.[11,12] In the biological milieu, there is dissolution of MNPs and dissociation in the acidic endolysosomes into the multivalent metal ions ($Mn^{2+}/Mn^{3+}/Mn^{5+}/Mn^{7+}$, Co^{2+}/Co^{3+}, Fe^{2+}/Fe^{3+}) which subsequently react with hydrogen peroxide (H_2O_2) and oxygen (O_2), generating ROS *via* the Fenton-like reaction.[13] ROS formation mediated by MNPs increases cellular oxidative stress, resulting in damage to cells and cellular components such as protein denaturation, mitochondrial damage, cell cycle arrest, and DNA/chromosomal damage.[14,15]

The majority of methods used to resolve the toxicity concerns associated with MNPs concentrate mostly on improving their stability in physiological media, systemic circulation by means of functionalization and/or coating with various

Department of Biomedical Engineering, Indian Institute of Technology Hyderabad, Kandi, Telangana, India. E-mail: enarm@bme.iith.ac.in, jgiri@bme.iith.ac.in

†Electronic supplementary information (ESI) available. See DOI: https://doi.org/10.1039/d2nr05218k

‡These authors equally contributed to this work.

materials such as polyethylene glycol (PEG),[16] silica,[17] albumin, dextran[18] and chitosan *etc.*[19,20] However these approaches have resulted in limited improvement of the IC_{50} value of Fe_3O_4 ranging from 0.1 to 100 μg, which further depends on several parameters such as incubation times, and the physicochemical properties of MNPs and cell lines.[21,22] The limited success is mainly attributed to the fact that these coated polymers finally degrade and eventually expose the metal oxide nanoparticles to biological systems with eventual ROS generation. On the other hand, quenching of ROS generated from MNPs in biological conditions simultaneously would be the most effective approach to reduce the toxicity of MNPs. In fact, as proof of concept, Mai *et al.*, and Ansari *et al.* reported[23,24] the significant quenching of ROS-induced stress of MNPs and improvement of their toxicity in the presence of antioxidant molecules and antioxidant polymers[15] along with MNPs, respectively. However, in order to improve MNP toxicity significantly, coatings containing ROS-quenching polymers that provide continuous quenching of ROS under biological conditions need/are yet to be developed.

Drug delivery systems with MNPs/nanocarriers and different drug molecules have tremendous applications for various diagnostic and therapeutic applications such as targeted delivery, imaging, chemo-hyperthermia, and chemo-photothermal therapy.[25,26] Moreover, synergistic use of magnetic hyperthermia (MHT) and chemotherapy for treating cancer using a co-delivery system of MNPs and chemotherapy drugs holds a great prospect in cancer therapy.[27] However, several limitations related to magnetic nanocarriers such as loading of drugs, targeted tumor accumulation, biodegradation and their toxicity are yet to be addressed.[28] Apart from magnetic targeting, stimuli-responsive (*i.e.*, ROS, temperature, enzyme and pH) magnetic nanocarriers can further enhance the site-specific controlled release of drugs and ultimately drug efficacy.[29] ROS are the major pathological stimulus in many chronic disease conditions including cancer.[30] To this effect, ROS-responsive nanocarriers and drug delivery systems are most promising for target site (such as tumor or tumor microenvironment *etc.*) specific delivery to reduce the off-target drug release and their side effects and improve therapeutic efficiency.[31–34] Among the different polymers used in drug delivery systems, polypropylene sulphide (PPS) has been considered as most promising due to its excellent biocompatibility, biodegradability and adequate ROS-responsive behaviour.[35,36] Our hypothesis of ROS-quenching biodegradable PPS-polymer coating on MNPs to make novel magnetic nanodelivery system could be a "one for all solution" where the PPS matrix simultaneously stabilizes the MNPs with tailored physicochemical properties, provides an excellent matrix for different drug loading, improves MNP toxicity significantly by continuously quenching the ROS from MNPs in biological systems (*in vitro* and *in vivo*) and provides ROS-responsive smart release of drugs at the target site for combination chemo-hyperthermia therapy for cancer.

To validate our hypothesis, we have used three different MNP systems (Fe, MnFe, CoFe) with different ROS generation potentials and coated with PPS polymer. The PPS-coated magnetic nano-delivery system was further investigated for (1) improved toxicity by 2-to-3 fold (highest compared with the reported value), (2) a versatile system to load different drugs, doxorubicin and curcumin, (3) ROS + pH responsive (multi-stimulus-responsive delivery), (4) hyperthermia at 45 °C and (5) combined chemo-hyperthermia of cancer with 95% killing efficacy. To the best of our knowledge, we are the first to report such a novel PPS-coated platform on MNPs by addressing several challenges together to make a smart, dual stimulus-responsive, biodegradable and excellent biocompatible magnetic-delivery system for chemo-hyperthermia application. This system can be adapted to other metal/metal–oxide NP systems to improve their biocompatibility by several orders of magnitude while still enabling smart ROS-responsive disease-targeted release for various biomedical applications.

2. Materials & methods

2.1 Materials

Iron acetylacetonate (99%), manganese acetylacetonate (99%), cobalt acetylacetonate (99%), propylene sulphide, 0.5 M sodium methoxide (NaOMe), Pluronic F127, hexadecandiol and benzyl ether were procured from Sigma-Aldrich. Oleic acid and oleylamine were purchased from TCI. Borax potassium thiocyanate (KSCN), 3,3′,5,5′-tetramethylbenzidine (TMB) and 2,2-diphenyl-1-picrylhydrazyl (DPPH) were purchased from SRL, India. Milli-Q water was used throughout all the experiments.

2.2 Synthesis of magnetic nanoparticles (MNPs)

Different types of MNPs such as Fe, MnFe and CoFe were prepared by following the previously reported seed-mediated high-temperature decomposition method.[37,38] Briefly, metal acetylacetonate (700 mg), oleic acid (2.3 mL), allyl amine (2.8 mL), hexadecandiol (2.5 g) and phenyl ether (25 mL) were added into a three-neck round bottle flask and maintained with stirring at 200 °C under nitrogen flow for 2 h. Thereafter the temperature of the mixture was raised to 300 °C and maintained for 1 h under a nitrogen blanket. The formed MNPs were magnetically separated and washed with a mixture of ethanol and hexane (2 : 1 volume ratio) and dried at room temperature for further use. The size of the above prepared MNPs was 4 nm. MNPs of size 8 nm, 12 nm and 16 nm were prepared by the seed-mediated method where 80 mg preformed NPs of 4 nm, 8 nm and 12 nm were used as seeds with the abovementioned precursors to get 8 nm, 12 nm, and 16 nm sized NPs respectively. Similarly, MNPs of MnFe and CoFe were prepared using a stoichiometric molar ratio of (2 : 1) for iron acetylacetonate, and manganese acetylacetonate or cobalt acetylacetonate.

2.3 Preparation of PPS-coated magnetic nanoparticles (PPS-MNPs)

PPS-coated magnetic nanoparticles (PPS-MNPs) were synthesized by anionic polymerization of propylene sulphide

monomer in the presence of Pluronic F127 as surfactant and pentaerythritol tetrathioester as initiator.[36] In the typical procedure, 3 mL of Milli-Q water containing borax as base and Pluronic F127 as surfactant was prepared and purged with N_2 followed by the addition of propylene sulphide (PS) into this solution. MNPs (of size ~16 nm) were dispersed separately in toluene and added to the above reaction mixture and sonicated for 20 min. Separately activated pentaerythritol tetrathioester initiator was further added into the reaction mixture and maintained for 24 h on shaking to complete the polymerization and generation of PPS NPs. PPS-MNPs were purified using a 100 kDa dialysis membrane for 2 days and stored at 4 °C for further characterization studies. Plain PPS NPs were prepared using same procedure as mentioned above except without the MNPs.

Dimercaptosuccinic acid (DMSA) coated MNPs (DMSA-MNPs) were prepared by exchanging the surface oleic acid of the hydrophobic MNPs with DMSA to get water-dispersible NPs as per a previous report.[39] The amount of MNPs in the PPS-MNPs was estimated by the metal ion titration method. Briefly, the PPS-MNPs were digested using HCl for 1 h for the complete dissolution of MNPs and the resultant solution was further mixed with ammonium persulfate (10 mg mL^{-1}) and potassium thiocyanate (1.5 M) to get a red color solution of iron thiocyanate complex. The absorbance of this solution was measured by a UV-Vis spectrophotometer at 480 nm to estimate the concentration of metal ions in the solution from the standard curve (Fig. SI 3b–d†) for known concentrations of iron (5, 10, 15 and 20 μg mL^{-1}).

2.4 Synthesis of drug-loaded ROS-responsive PPS-coated magnetic nanoparticles (PPS-MNP drug NPs)

Doxorubicin (DOX) and curcumin (CUR) were used as model anticancer drugs for the preparation of drug-loaded PPS-MNPs. An *in situ* drug-loading process was used for the preparation of the drug-loaded PPS-MNPs. Briefly, the hydrophobic drugs DOX or CUR were dissolved in chloroform and added to the reaction mixture containing an aqueous solution of borax and Pluronic F127 followed by the addition of the PS monomer. DOX (doxorubicin HCl) was converted from hydrophilic to hydrophobic form by the addition of trimethylamine to a chloroform solution of DOX to prepare DOX-loaded PPS-MNPs. Similarly, only drug-loaded PPS NPs were also prepared without magnetic particles. As DOX is unstable under oxidative conditions for longer durations of time, we have used CUR instead to monitor the release profile of drug under an *in vitro* oxidative setting.[40]

2.5 Physicochemical characterization studies

2.5.1 Measurement of hydrodynamic particle size and zeta potential. The hydrodynamic particle size and zeta potential of prepared NPs were analyzed by a dynamic light scattering (DLS) technique using a Zetasizer Nano ZS (Malvern, UK) at a fixed angle of 170 degrees at 25 °C. The DLS measurements were done using an aqueous dispersion of samples (100 μL mL^{-1}), whereas diluted PBS 7.4 (0.01 M) was used for the zeta potential measurements. Each result represents the mean ± standard deviation of three measurements with 20 runs for each sample.

2.5.2 Transmission electron microscopy (TEM) analysis and scanning electron microscopy. The particle size and morphology of the NPs were determined by transmission electron microscopy (TEM, 2100 JEM, Jeol, Japan) at 80 kV voltage. 10 μL of well-dispersed samples was drop-casted on a carbon-coated copper grid and dried at room temperature before analysis under microscope.

2.5.3 Fourier transform infrared spectroscopy (FTIR) analysis. Different functional groups and bonding in lyophilized samples were analysed by a FTIR spectrometer Alpha-II (Bruker instrument, Germany) and performed in attenuated total reflection (ATR) mode in the scan range of 4000 to 400 cm^{-1}. The scan was set at 16 with 2 cm^{-1} resolution steps. The graphs were plotted using OriginPro software v. 9.1.

2.5.4 X-ray diffraction (XRD) analysis. The crystalline structure of powdered NPs was studied by XRD analysis using an X-ray diffractometer (Ultima-IV, Rigaku, Japan) with radiation of (40 kV/40 mA) in the 2θ range of 20° to 80°. The average crystalline size was estimated using the Debye–Scherrer equation, $D = 0.9\lambda/\beta\cos\theta$, where D is the crystalline size, λ is the wavelength of the X-ray, β is the full width at half maxima (FWHM), and θ is Bragg's angle.

2.5.5 Vibrating-sample magnetometer (VSM) analysis. Magnetic properties of the lyophilized samples of different MNPs and PPS-coated MNPs were studied by VSM (Model 7407, LakeShore, USA) using fields up to 1.5 T at room temperature.

2.5.6 Thermogravimetric analysis (TGA). TGA analysis was done to study the thermal stability and to quantify the percentage of different components in the samples. Freeze-dried samples (~2 mg) were placed in a TGA instrument (SDT Q 600, TA instrument, New Castle, Delaware, USA) in the temperature range of 30 to 700 °C with a 10 °C min^{-1} heating rate under continuous nitrogen gas flow (100 mL min^{-1}).

2.5.7 Calorimetric magnetic fluid hyperthermia measurements. Magnetic hyperthermia studies of dispersed MNPs and MNP-incorporated PPS NPs were carried out using the MagneTherm™ instrument (NanoTherics, UK). The frequency and applied alternating magnetic field (AMF) of the instrument can be varied in the range from 177 kHz–1017 kHz and 12 mT–20 mT respectively. Different MNPs (Fe, MnFe, CoFe) were analysed for their heating ability, and SAR (specific absorption rate) and ILP (intrinsic loss power) values were calculated by given eqn (1) and (2), where, C_p (specific heat capacity) is 4.18 J g^{-1} K^{-1}, D_c (density of colloid) at 25 °C is 0.997 g ml^{-1}, C_f is the concentration of the MNP, dT is the change in temperature (K) at the specific measurement time and dt is the first 20 s where the difference in temperature is measured. For the ILP value, f is the frequency *i.e.* 993 kHz and H is the intensity *i.e.*, 10 kA m^{-1} of the magnetic field.

$$\mathrm{SAR} = C_p \cdot \frac{D_c}{C_f} \cdot \frac{dT}{dt} \quad (1)$$

$$\mathrm{ILP} = \frac{\mathrm{SAR}}{fH^2} \quad (2)$$

Further PPS-MNPs were also checked for their heating ability and concentration-dependent studies were also performed to optimize the best concentration for *in vitro* applications.

For analysis, first a desired amount of the sample in a 2 mL tube was inserted inside a polystyrene holder to avoid temperature fluctuations and then fixed inside the coil (9/17 turns). The hyperthermia was measured at frequency 993 kHz for the different concentrations and different types of the NPs. The change in temperature was measured by the OSENSA single channel optic fibre with 10 s intervals from 25 °C to 46 °C and plots were prepared accordingly.

2.5.8 Drug encapsulation efficiency, loading capacity, and release profile with/without the presence of oxidative conditions. The encapsulation efficiency (EE) and loading capacity (LC) of the DOX and CUR loaded PPS-MNPs were determined by UV-Vis spectrophotometry and HPLC respectively. Briefly, 200 μL of the drug-loaded NPs was lyophilized and dichloromethane (DCM) solvent was added to the dried drug-loaded NPs to extract the DOX and CUR from the NP matrix. Furthermore, the obtained extract with the drug was dried and re-dissolved in a fixed volume of DMSO for DOX and acetonitrile in the case of CUR. Absorbance was recorded at a 480 nm wavelength using a UV-Vis spectrophotometer for DOX, and HPLC analysis was performed for CUR.[41] The amount of drugs was calculated using a standard plot of known concentrations of drug as shown in Fig. SI 4a and 5(a and b).† EE % and LC % were calculated using following eqn (3) and (4).

$$\mathrm{EE}\ \% = \frac{\text{Amount of drug loaded}}{\text{Amount of drug taken}} \times 100 \quad (3)$$

$$\mathrm{LC}\,\% = \frac{\text{Amount of drug loaded}}{\text{Amount of drug loaded NPs}} \times 100. \quad (4)$$

The *in vitro* release behaviour of DOX from NPs was determined by the dialysis method. Briefly, 10 mg mL^{-1} of the NP suspension in 1.5 mL of 1× PBS (pH 7.4) containing 0.1% (v/v) Tween 80 was filled into a dialysis tube of 14 kDa. The tube was further immersed in 10 ml of PBS and the release profile was determined under shaking conditions maintained at 37 °C and 100 rpm. At specific time intervals, 1.0 mL of drug-released medium was collected, followed by replacement with fresh 1× PBS to maintain the constant sink volume of 10 mL. The collected samples were analysed using a UV-Vis spectrophotometer and the amount of released drug was quantified using a standard curve of known DOX concentrations (2, 5, 10, 20 μg mL^{-1}) at 480 nm wavelength in DMSO as solvent.

Further to check the ROS-responsive release, we have used CUR as a model drug. For this study, 10 mg mL^{-1} of the NP suspension in 1.5 mL of 1× PBS was filled into the dialysis membrane. The NP-containing dialysis bag was suspended in 0, 5, or 50 mM H_2O_2 in 1× PBS (pH 7.4) and in an acidic pH 5 (containing 0.01% w/v butylated hydroxytoluene and 0.1% w/v *N*-acetylcysteine (NAC)) to check the ROS-responsive release of NPs in pH 7.4 and in an acidic environment pH 5, respectively.[42] At specific time intervals, 1.0 mL of drug-released medium was collected and replaced with fresh medium to maintain the constant sink volume of 20 mL. HPLC analysis was performed to plot the standard curve and determine the amount of released drug at 420 nm wavelength.

2.5.9 ROS-scavenging properties of PPS using peroxidase activity assay and DPPH assay. The peroxidase activity measurement was carried out by colorimetric assay using 3,3′,5,5′-tetramethylbenzidine (TMB) as substrate in the presence of the different NPs. PPS NPs, DMSA-MNPs and PPS-MNPs were dispersed in 0.1 M of acetate buffer (pH 4.8), and 200 μL of TMB substrate was added followed by the addition of 140 mM H_2O_2. After shaking for 30 min at room temperature, photographs of the developed blue color in the samples were taken and samples were further analysed by UV-Vis spectrophotometer (Jasco V-750, Japan) at 650 nm to compare the peroxidase activity.

To perform the DPPH radical-scavenging assay, DPPH was dissolved in a water : methanol (20 : 80) mixture to make a final concentration of 100 μM. To perform the experiment, 10 μL of each sample solution was added to 500 μL of freshly prepared DPPH radical solution and incubated at room temperature for 25 min. To check the radical-scavenging property of the samples, absorbance at 517 nm was measured using a UV-Vis spectrophotometer (Jasco V-750, Japan).

2.6 Biological studies

2.6.1 Cell culture. Human breast carcinoma cell line MCF7, murine fibroblasts NIH3T3 and human embryonic kidney cells HEK293 were cultured in Dulbecco's modified Eagle's medium (DMEM, High Glucose, Gibco) supplemented with 10% fetal bovine serum (Gibco) and 1% antibiotic solution, maintained under 5% CO_2 in a humidified atmosphere at 37 °C.

2.6.2 Intracellular uptake studies of PPS-MNPs. Doxorubicin-loaded PPS NPs (PPS-MnFe-Dox) were used to measure their uptake into MCF7 cells by flow cytometry according to the reported protocol.[43] Briefly, 10^5 cells per well were seeded in a 12-well plate and allowed to attach overnight. Then, cells were incubated with PPS-DOX NPs at an equivalent DOX concentration of 1 μg mL^{-1} for 0.5, 1 and 3 h. After incubation, the cells were washed with 1× PBS and collected by enzymatic dissociation using trypsin. The collected cells were washed with 1% BSA–PBS twice and kept on ice until flow cytometric evaluation was done.

The intracellular uptake of PPS-MNPs was qualitatively determined by fluorescence microscopy and Prussian blue staining. Briefly, cells were seeded at a concentration of 10^3 cells per well on a coverslip and allowed to grow for 24 h and subsequently treated with 100 μg mL^{-1} of PPS-MNPs for 6 h. After the incubation period, the cells were fixed in 4% paraformaldehyde for 20 min followed by two times washing with 1× PBS. Cells were stained with 4% Prussian blue staining solution in HCL for 30 min and washed thoroughly.

For fluorescence visualization, the PPS-MnFe-DOX NPs were incubated with MCF7 cells (10^3 cells per well) for 3 h. After the incubation, the cells were washed twice with 1× PBS to remove non-internalized particles. The cells were then counterstained with Hoechst 33342 (10 μg mL^{-1}) for 10 min. Finally, cells were imaged on an inverted microscope (Olympus 1X73, Japan) to confirm the uptake. Brightfield images were collected for Prussian blue stained samples and fluorescent images were acquired for PPS-MNP-DOX treated samples.

2.6.3 Cell viability assessment by MTS assay. The MTS (3-(4,5-dimethylthiazol-2-yl)-5-(3-carboxymethoxyphenyl)-2-(4-sulfophenyl)-2*H*-tetrazolium) assay was employed to determine the effects of magnetic particles and PPS-MNPs on the cellular viability of NIH3T3 and HEK293 cells. Briefly, cells (10^3 cells per well) were seeded in 96-well plates and allowed to attach overnight. The old medium was discarded and replenished with fresh medium (untreated control) and medium with bare and PPS-MNPs (M = Fe, MnFe, CoFe) at the indicated concentrations (0–1000 μg mL^{-1}) and were maintained at 37 °C for 24, 48 and 72 h. The delivery vehicle (plain PPS NPs) were also incubated with the two cell lines for concentrations ranging from 0–3 mg mL^{-1} for 24, 48 and 72 h. After treatment for specific time points, the supernatants were removed, and the cells were washed with 1× PBS, and incubated with 20% MTS solution in complete medium for 3 h. Thereafter, the supernatants were collected and transferred to a fresh 96-well plate for reading. The absorbance was measured on an iD5 Multi-Mode Plate Reader (Molecular Devices, USA) at 490 nm and reference wavelength at 600 nm. Viability was calculated as:

$$\text{Viability}\,\% = \frac{(\text{Absorbance of treated group} - \text{Absorbance of blank})}{(\text{Absorbance of untreated group} - \text{Absorbance of blank})} \times 100$$

2.6.4 Intracellular ROS scavenging by PPS NPs. NIH3T3 cells were plated in a 96-well plate at a density of 10^4 per well for 12 h. After the medium was removed, the cells were pre-incubated with DMEM containing 10% FBS and PPS NPs (50 and 100 μg mL^{-1}) for 12 h. The cells were washed with 1× PBS to remove excess PPS NPs and then incubated with DMEM containing 10% FBS and hydrogen peroxide (125, 250 and 500 mM). A total of 1 h later, the cell medium was replaced with DCFDA followed by incubation for 30 min at 37 °C in the dark. The group without any treatment was defined as the control. For comparison, *N*-acetylcysteine (NAC) was used as a known ROS scavenger in this study. Briefly, plated cells were pretreated with DMEM containing 10% FBS and NAC (5 mM) for 30 min, followed by the addition of hydrogen peroxide. After the respective treatments, excess DCFDA was removed and cells were supplemented with 1× PBS before reading (Ex-485 nm/Em-535 nm) on an iD5 Multi-Mode plate reader (Molecular Devices, USA).

The same experimental procedure was carried out in parallel to enable qualitative assessment using fluorescence microscopy. After the addition of the DCFDA reagent, the cells were counterstained with Hoeschst 33342 for 5 min. The cells were thereafter imaged on an inverted fluorescence microscope (Olympus 1X73, Japan).

2.6.5 *In vitro* magnetic hyperthermia. *In vitro* magnetic hyperthermia (MHT) studies were performed using PPS-MnFe and PPS-MnFe-DOX NPs. Herein, 1×10^6 breast (MCF-7) cancer cells in DMEM medium were suspended with PPS-MnFe-DOX particles at a concentration of 2 mg mL^{-1} (MNP equivalent). They were then subjected to an AMF of 993 kHz to reach the therapeutic temperature (45 °C), which was further maintained for 15 min by attuning the AMF. In addition, an equal number of cells were subjected to the following treatments: (i) free doxorubicin corresponding to an equivalent concentration of 2.75 μg mL^{-1}, (ii) only PPS-MnFe particles at a 2 mg mL^{-1} concentration and (iii) cells without any treatment. After MHT treatment, approximately 5×10^4 cells (corresponding to ~50 μL of cell suspension) were mixed with 1 mL of DMEM (containing 10% FBS) and plated in triplicate in a 48-well plate, followed by 24 h of incubation at 37 °C under 5% CO_2. A similar procedure was followed for all treatment groups without applying AMF and cells were subjected to AMF only. Finally, the MTS assay was performed to determine the viability of the cells. After washing with 1× PBS twice, brightfield microscopic images were acquired to determine the morphology of the treated cells.

2.6.6 Determination of the cell death mechanism. Following MHT, as a quantitative assessment of cell apoptosis induction, annexin V staining was performed, where 5×10^5 cells were taken immediately after hyperthermia treatment, stained with annexin V (Invitrogen, USA) reagent according to the manufacturer's instructions and proceeded to flow cytometry (BD FACSCelesta, USA).

Additionally, a similar set of cells subjected to the aforementioned MHT treatment were stained with calcein AM (2 μM) to qualitatively estimate the live cell population by fluorescence microscopy. Briefly, after the MHT treatment, cells from the respective groups were seeded on a 48-well plate. After 24 h of cell attachment, the cells were stained with calcein AM to determine the fraction of live cells remaining. For both the assays, staining with propidium iodide (PI) was not performed to avoid the fluorescence overlap with the DOX signal simultaneously.

2.7 Statistical analyses

All data are shown as means ± standard deviation (SD) and statistically evaluated using Origin 8 and GraphPad Prism 9 software using ANOVA. Image analyses were carried out on ImageJ software (NIH). Flow cytometry data were analysed on FlowJo software (BD, USA).

3. Results and discussion

3.1 Magnetic nanoparticles and PPS-coated formulations (PPS-MNPs)

MNPs have been widely used for the past few decades in various biomedical applications due to their unique and

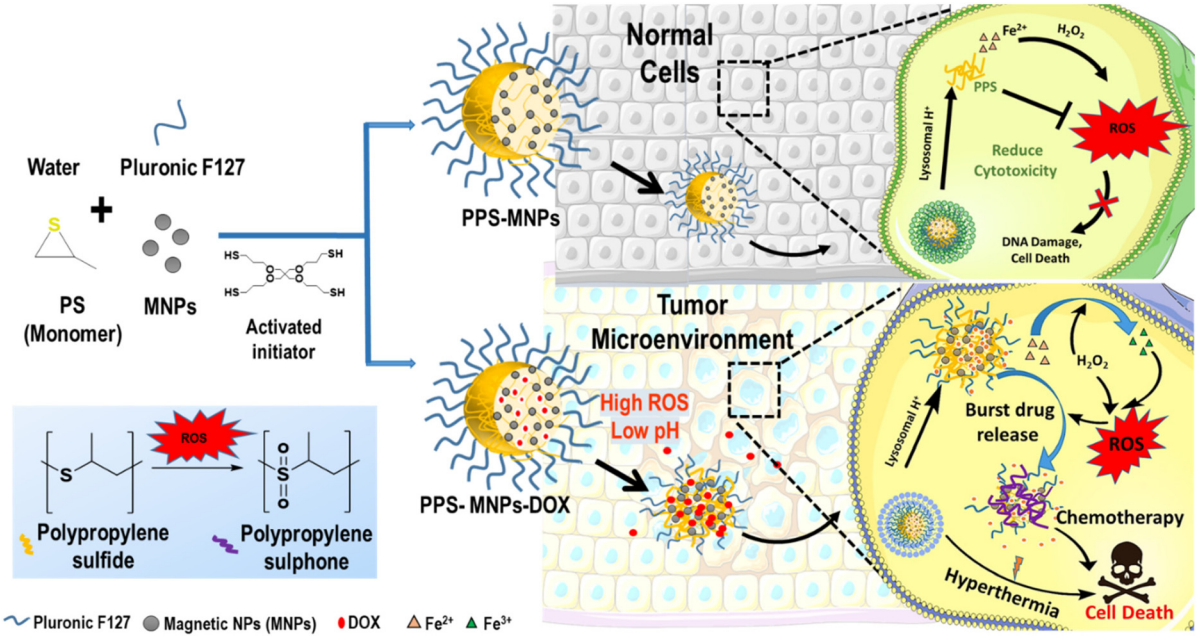

Fig. 1 Schematic representation of the synthesis of PPS NPs and application as drug delivery vehicles in cancer treatment. PPS improves the biocompatibility of the MNPs in healthy cells by quenching the ROS which are produced by MNPs. However, in the tumor microenvironment where an oxidative acidic environment is maintained, PPS undergoes degradation thereby releasing the drugs and along with hyperthermia is useful for the combined chemo-hyperthermia therapy of cancers.

superior chemical, biological and magnetic properties. However, concern has arisen regarding the performance of MNPs in physiological circumstances, *in vivo* and *in vitro*, due to their toxicity mainly related to the excess generation of ROS. To overcome this limitation, PPS-coated MNPs (PPS-MNPs) were prepared, where PPS polymer could quench the ROS, generated by the MNPs under physiological conditions. Furthermore, these PPS-MNPs were explored as drug-loaded nanocarriers which could release the drug in a dual stimuli-responsive manner: low pH and oxidative conditions for disease site-specific targeted delivery (Fig. 1). To achieve these objectives, different types of MNP with varying ROS generation capacity, such as Fe_3O_4 (Fe), $MnFe_2O_4$ (MnFe) and $CoFe_2O_4$ (CoFe) of 16 nm, were prepared by a seed-mediated high-temperature decomposition method and further coated with or incorporated into PPS matrix to obtain PPS-Fe/MnFe/CoFe NPs using an anionic polymerization emulsion method. The PPS polymer matrix easily incorporates the hydrophobic MNPs inside the core where several magnetic particles incorporate in one particle and are further stabilized with Pluronic F127, providing a hydrophilic particle surface. PPS polymer contains thiol groups which further bind to the surface of the MNPs by replacing the oleic acid coating from the surface and improving the stabilization of the NPs within the PPS polymer matrix. PPS-MNPs possess a high loading efficiency of MNPs. These PPS-MNPs were checked for improved biocompatibility, dual stimuli-responsive drug release, and hyperthermia applications discussed below. PPS, being a ROS-sensitive polymer, can consume the ROS species and is expected to reduce the oxidative stress-related toxicity from MNPs in the human body as well as the micro-environment (low pH and high ROS) responsive release of the drug compared with the normal physiological conditions (see below).

3.2 Particle sizes and surface charge of different NPs

TEM micrographs of bare PPS NPs and PPS-MNPs (MnFe) are shown in Fig. 2(a–d). TEM images of bare MnFe NPs (Fig. 2a) show monodispersed, nearly spherical nanoparticles of ~14 ± 2 nm size. TEM analysis has also confirmed that Fe and CoFe NPs prepared by a similar method are of same size as shown in Fig. SI 1(a and b).† The appearance of a characteristic ring pattern in the obtained SAED pattern of PPS-MnFe NPs (inset of Fig. 2a) indicated the formation of crystalline spinel cubic MnFe which is in good agreement with the XRD data (ESI Fig. 4a†) discussed below. TEM analysis (Fig. 2b) of PPS NPs showed the formation of monodispersed and spherical-shape particles having a diameter of ~80 nm. Fig. 2(c and d) show high-resolution TEM micrographs of PPS-MNPs and it was observed that the particles are spherical in shape having an average size of 80 ± 15 nm and the same was confirmed by SEM as shown in Fig. SI 1(c and d).† The high-resolution image clearly shows a light grey coating of thickness ~6 ± 1 nm of amorphous polymer around the relatively darker MnFe NPs, confirming the presence of PPS polymer (Fig. 2d). It also shows the presence of well-ordered atomic planes having characteristic crystal lattices on the MnFe NPs, suggesting their crystallinity. Thus, it indicates that the coating process has not altered the crystalline nature of the MNPs, which determines their magnetic properties, and MNPs are in the form of a cluster encapsulated inside the core of the PPS

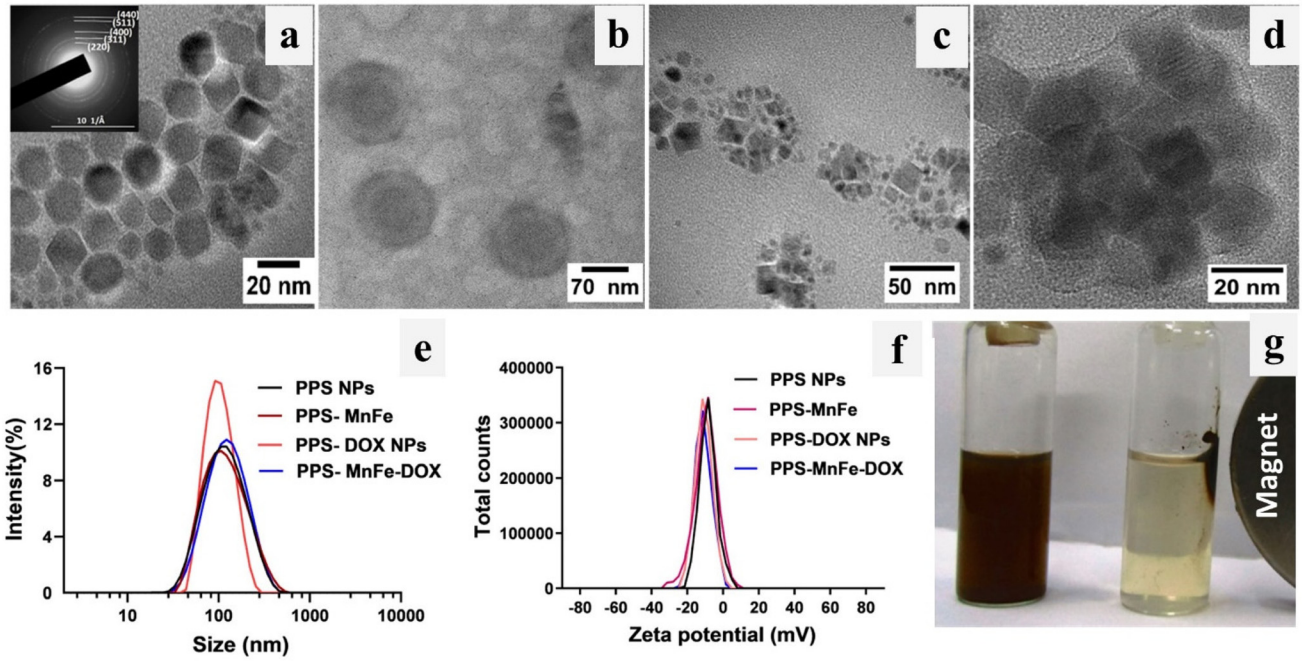

Fig. 2 Physicochemical characterisation of different NPs. TEM images of (a) MnFe NPs and (b) PPS NPs; (c) TEM images of PPS-MnFe NPs of size 80 ± 15 nm and multiple MNPs encapsulated in PPS polymers; (d) higher magnification TEM images of PPS-MnFe NPs, where the distribution of multiple MNPs encapsulated in the core of the PPS polymers MNPs has been observed. (e) Gaussian distributions of the hydrodynamic diameter size distribution of (100 nm) PPS NPs, PPS-MnFe NPs, PPS-DOX NPs, and PPS-MnFe-DOX NPs. (f) Zeta potential (surface charge) of PPS NPs, PPS-MnFe NPs, PPS-DOX NPs, and PPS-MnFe-DOX NPs. (g) PPS-MNP behaviour and magnetic property in the presence of an external magnet. The dark brown color vial (left side) shows the well-dispersed NPs; however in the presence of an external magnet (right side) all the NPs were attracted toward the magnet and formed a cluster.

polymer. The different composition of PPS-MNPs *i.e.* MnFe, CoFe and Fe NPs was further confirmed with the help of energy dispersive spectroscopy (EDS) mapping and shown in Fig. SI 1e.† The EDS elemental analysis illustrates the presence of the different metals (Fe, Mn, and Co) and the presence of sulfur in the nanocomposite confirms the PPS-MNP formation. For drug delivery applications of NPs, it is very important to analyse the hydrodynamic particle size and zeta potential of the nanoparticle dispersion and stability in biological environments. Hydrodynamic particle sizes and zeta potentials of PPS NP, PPS-MnFe, PPS-DOX NPs, and PPS-MnFe-DOX NPs dispersions were evaluated by the DLS technique and the obtained particle size distribution results are shown in Fig. 2(e and f).

It is observed that all the NPs have a single and narrow particle size distribution. The hydrodynamic particle size and zeta potential value of MnFe-incorporated PPS NPs (PPS-MnFe NPs) were found to be 90 ± 13 nm and −12 ± 2 mV (ESI Table 1†). The PDI value of NPs (0.190 ± 0.007) indicated excellent monodispersity of PPS-MnFe NPs as confirmed by TEM analysis as well (Fig. 2c). As expected, the hydrodynamic size of NPs is higher than the size obtained from TEM.[44] These DLS and TEM analyses demonstrate the multiple MNPs inside the PPS polymer matrix of PPS-MNPs, which is further confirmed by the SEM analysis as shown in Fig. SI 1c.† Drug-loaded PPS-MNP systems (plain PPS NPs, PPS-MnFe NPs, PPS-DOX NPs and PPS-MnFe-DOX NPs) also show a nearly similar range of hydrodynamic size and zeta potential values as shown in ESI Table 1.† The relatively low negative surface charge of these PPS-based nanoparticles with excellent stability indicated that the hydrophilic Pluronic F127 groups act as surface stabilizing agents around the PPS matrix, which is further confirmed using FTIR (see below). Similarly, other MNPs (Fe and CoFe) of 16 nm size were also prepared and TEM images are shown in the images of Fig. SI 1(a and b).† To check the presence of different metal ions in different ferrites (Fe, Mn, and Co). EDS was performed and shown in Fig. SI 1e,† which confirmed the presence of the metals in the respective MNPs and the composition of different metal ions (Fe, Mn and Co). TEM, SEM, EDS and DLS of other MNPs and PPS-MNPs confirm the coating of PPS polymer on the MNPs.

3.3 Stability of NPs in different media and temperatures

The stability of the PPS-MnFe NPs was studied under different conditions such as in different media (water, PBS, and biological media) at 7.4 pH and different temperatures (25, 37 and 46 °C) in order to observe the NPs' behaviour in the simulated physiological environment (*in vitro* and *in vivo*) and hyperthermia condition (42–46 °C). Fig. 2g shows the digital photographs of the PPS-MnFe NPs' dispersion in water, and their response under a magnetic field. It was observed that PPS-MnFe NPs are well dispersed and respond to the magnetic field to accumulate on the magnet and redisperse in the

absence of a magnetic field without a change in hydrodynamic size. This magnetic field response is useful for magnetic targeted delivery and imaging-guided-based drug delivery.[45] Furthermore, from a temperature-dependent stability study, it was observed that PPS-MnFe NPs are stable at different temperatures (25, 37 and 46 °C) as no significant changes in the particles' size (hydrodynamic diameter) were observed, which varied between 114 nm (25 °C) to 105 nm (46 °C). This slight reduction in size with temperature could be attributed to the shrinking of the thermo-sensitive Pluronic F127[46] (Fig. SI 2a–b†). Lower PDI values (0.24 to 0.16) at these temperatures also indicated the monodispersed and stable nature of PPS-MnFe NPs. These particles were further checked for serum stability for 24 h as shown in Fig. SI 2(c and d).† Particles were found to be stable in DMEM containing 10% FBS, as no significant differences in particle size were observed for 6 h. After 24 h of incubation in DMEM with 10% FBS, the particle size of PPS-MnFe NP increased to nearly double due to possible protein corona formation on the surface of the nanoparticles.[47] These NPs showed excellent stability in different media and temperature conditions. This observed stability of PPS-MnFe NPs can be attributed to the synergistic contributions of the electrostatic repulsion between the particles due to the negative charge (zeta potential −9 ± 1.3 mV) on the surface and steric hindrance due to the presence of the PEO chain of the Pluronic surfactant. The negative surface potential and hydrophilic surface functional groups on the particle surface are thought to be responsible for the excellent stability under physiological and hyperthermia conditions.

3.4 Crystallinity and coating of different NPs

XRD analysis was carried out to study the crystalline structure, and phase purity of different types of prepared PPS-MNP (Fe/MnFe/CoFe), and to confirm the formation of PPS-MNPs. Fig. SI 4a† shows the XRD patterns of bare and PPS-MNPs (Fe, MnFe and CoFe). The XRD patterns show the presence of characteristic peaks of spinel cubic MnFe (JCPDS No.: 10-0319), CoFe, (JCPDS No.: 22-1086) and Fe (JCPDS No.: 88-0866) and the obtained patterns are well matching with the reported literature.[48] The crystallite sizes calculated by the Debye–Sherrer equation of MnFe, CoFe, and Fe NPs were found to be between 14 nm to 16 nm. A relatively reduced intensity in the case of PPS coating has been observed in all cases of PPS-MNPs, which could be attributed to the reduced amount of crystalline magnetic phase in the final nanocomposite compared with the pure MNPs. The presence of characteristic reflection peaks of crystalline spinel cubic MnFe, CoFe, and Fe in the XRD patterns of PPS-coated nanocomposites confirms the formation of PPS-MnFe, PPS-CoFe and PPS-Fe nanocomposites and also indicates that the chemical coating process of PPS on MNP does not adversely affect or alter the crystalline nature of the MNPs.

3.5 FTIR analysis

FTIR analysis of oleic acid-coated MnFe NPs (OA-MnFe NPs), PPS NPs and PPS-MnFe-NPs was carried out to verify their chemical composition, and surface chemical properties, depicted in Fig. 3a. The vibrational spectra of OA-MnFe have shown a band at around 500 cm^{-1}, which can be attributed to vibration of the Fe–O bond related to MnFe NPs. The bands in the IR spectra of OA-MnFe at 1550 and 1400 cm^{-1} can be assigned to asymmetric and symmetric stretching variation of the COO^- group of the oleic acid, which got shifted down from 1715 cm^{-1} due to the bridging bidentate-type binding between the NPs' surface metal ion and the COO^- groups of the oleic acid.[49] In the case of PPS NPs, the appearances of characteristic bands at 1100 cm^{-1} for the C–S bonds of PPS and at 2900 cm^{-1} for the C–H bonds of the PPS confirm the presence of the PPS polymers and suggest the successful formation of PPS NPs.[50] PPS-MnFe has shown three characteristic peaks, one at 500 cm^{-1} confirming the presence of the Fe–O of MnFe and other peaks at 1100 cm^{-1} and 2900 cm^{-1} due to the C–S bonds and C–H bonds respectively, confirming the presence of the PPS polymer in the nanocomposite. Two bands at 1550 and 1400 cm^{-1} are missing in the FTIR spectra of PPS-MnFe-NPs compared with OA-MnFe, suggesting a complete exchange of the oleic acid with the PPS polymer. The band of PPS at 1676 cm^{-1}, which is due to the iodoacetamide capping of the reactive thiolate (S^-), disappeared in the FTIR spectrum of PPS-MnFe NPs, implying that the PPS thiol (SH or S^-) was bound on the surface of the MNPs in the form of Fe–S covalent bonds.[51] These analyses give evidence of PPS binding through reactive thiolate bonding with the surface of MNPs; hence, no reactive thiolate remains in the PPS to be capped with iodoacetamide. Therefore, FTIR data confirmed the successful formation of OA-MnFe, PPS NPs and PPS-MnFe NP. FTIR also confirms that the oleic acid coating of OA-MnFe is successfully exchanged with the PPS coating in PPS-MnFe NPs.

3.6 Thermogravimetric analysis (TGA)

TGA analysis of oleic acid (OA), DMSA and PPS-MNPs were carried out to confirm the coating, and structural changes related to temperature alteration, and to calculate the %age of encapsulated MNPs in the nanocomposite samples. The analysis was carried out from 30 °C to 800 °C and the obtained results are given in Fig. 3b. A slight weight loss of ~1–4% below 150 °C in all the samples was observed and can be attributed to the loss of water molecules. Weight losses of ~12% and ~15–16% in between 150 to 600 °C in the case of OA-MnFe NPs and DMSA-coated MNPs (MnFe, CoFe, and Fe NPs) respectively, are related to the loss of the oleic acid and DMSA coating. This difference of ~4% more weight loss in the case of DMSA-coated samples than the OA-MnFe NPs indicates the coating of the DMSA on the OA-MNPs. All PPS-MNPs have shown a significant weight loss of 60–70% in between 200–500 °C, which can be attributed to the loss of coated organic materials (Pluronic F127 and PPS polymer). Thus, the TGA results along with the TEM observations validate the coating and presence of PPS polymer in the PPS-MNP samples. From the TGA results, the amount of the MNPs in the PPS-MNP was found to be ~30–40% (w/w) of PPS, which nearly correlates with the value obtained from the VSM data.

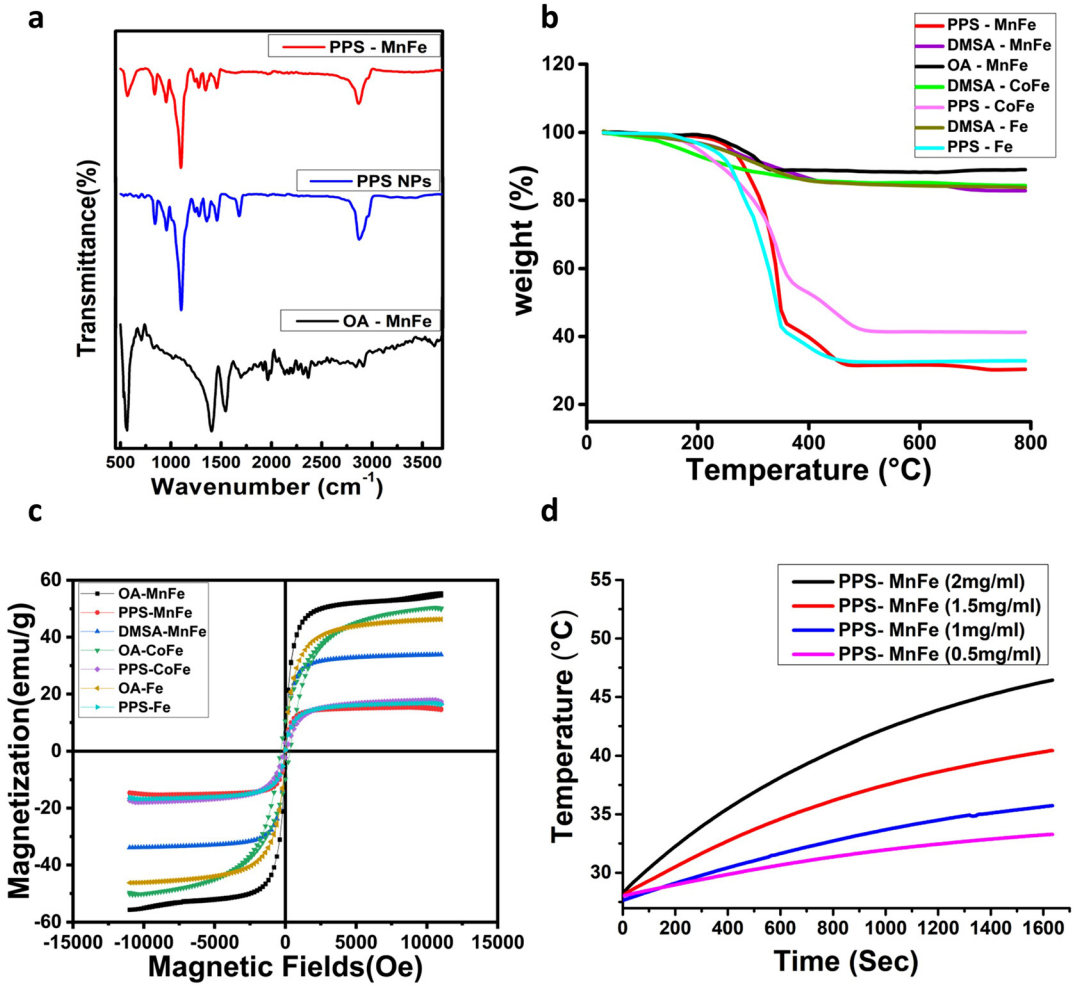

Fig. 3 Chemical and magnetic characterisation. (a) FTIR characterisation of plain MNPs (OA-MnFe), PPS NPs and PPS-MnFe NPs. Peaks attributed to MNPs at 500 cm^{-1} (Fe–O) are present in both the OA-MnFe and PPS-MnFe NPs graphs, and a peak at around 1100 (C–S) present in both the PPS NPs and PPS-MnFe NPs confirms the formation of NPs and PPS-MnFe. (b) Thermogravimetric analysis (TGA) graph presenting the % weight reduction during the melting of different coatings of OA, DMSA and PPS polymers. PPS-MNPs showed more % weight reduction compared with OA- and DMSA-coated MNPs. (c) Magnetization curve (magnetic hysteresis (M–H) loop) shows the saturation magnetization (M_s) of OA-MNPs, PPS-MNPs and DMSA-MnFe NPs. These curves show the superparamagnetic behaviours of NPs, which reduced in the case of PPS-MNPs. (d) Response of the PPS-MnFe NPs with varying concentrations (0.5–2 mg mL^{-1}) to an external AMF using a 993 kHz frequency. This graph shows that the 2 mg mL^{-1} concentration is working better and can achieve a temperature raise from 28 °C in 46 °C in 25 min, wherein to attain a temperature rise from 37 °C to 42 °C, NPs took less than 10 min.

3.7 Magnetic properties of PPS-MNPs

The room temperature *M–H* curve of MnFe, Fe, and CoFe NPs (~16 nm size) and their corresponding PPS-MNPs and DMSA-MnFe NPs are shown in Fig. 3c and an enlarged image is shown in ESI Fig. 4b.† MnFe NPs, both in their bare form and in coated form *i.e.* DMSA-MnFe or PPS-MnFe NPs, show superparamagnetic behaviour due to the presence of single domain-sized MnFe, which is a primary requirement for hyperthermia therapy and magnetic-based targeted drug delivery applications. The same behaviour was observed in the case of Fe and PPS-Fe NPs. However, it was observed that bare CoFe NPs (16 nm) and PPS-CoFe showed the presence of a small amount of coercivity (329.6 Os for bare MNPs and 110.5 Os for PPS-coated MNPs) and remnant magnetization (10 emu g^{-1} for bare MNPs and 2.8 -emu g^{-1} for PPS-coated MNPs). These results were obtained because bulk CoFe is known for its high coercivity and only a very small size particle of CoFe shows a superparamagnetic nature.[52] All the samples' coercivity and remnant magnetization (MR) were checked by plotting the hysteresis at low fields, shown in ESI Fig. 4b.† The coercivity (H_c) and remnant magnetization (M_R) values for DMSA-MnFe and PPS-MnFe and PPS-Fe NPs were found to be in between 1 to 9.6 Oe and less than 0.5 emu g^{-1}, respectively. The M_S (saturation magnetisation) values of MnFe, Fe, and CoFe NPs were found to be 55.4, 46.2, and 49.8 emu g^{-1} which is comparable to the reported method.[22] The M_S value for DMSA-MnFe NPs was 33.8 emu g^{-1}, whereas the M_s values for PPS-coated MnFe,

Fe, and CoFe MNP were found to be 14.4, 16.2 and 16.8 emu g^{-1}. The decrease in the M_s values in the case of DMSA and PPS coating compared with the corresponding bare MNP is due to the incorporation of a nonmagnetic component in the final nanocomposite. The amount of magnetic and polymer coating materials was found to be ~25–35 w% and 65–75 w% respectively, nearly in agreement with the values obtained by TGA (Fig. 3b). The M_s value of a magnetic nanocarrier represents its magnetic controllability and generally more than 7 emu g^{-1} is preferred for magnetically targeted drug delivery and hyperthermia applications.[53] The observed M_s (14.4 to 16.8 emu g^{-1}) of all prepared PPS-MNPs is sufficient enough for magnetically controlled drug delivery.

3.8 Calorimetric magnetic fluid hyperthermia measurement

In order to check the potential of the different NPs to be used in hyperthermia applications, we measured the SAR and ILP values of NPs from a time-dependent increase in the temperature curve in response to the external magnetic field at frequency 993 kHz and shown in ESI Table 2.† These results demonstrate that a 2 mg mL^{-1} concentration of DMSA-MnFe of NPs shows the highest SAR and ILP values, *i.e.* 214 and 2.16 respectively, compared with DMSA-Fe (SAR = 115 and ILP = 1.16) and DMSA-CoFe (SAR = 109 and ILP = 1.10). Previous reported articles show that the SAR value or heating ability depends mainly on the saturation magnetization (M_s) value and coercive field (H_c) value. MNPs with a high M_s, a larger response under the applied AMF and a lower H_c value show a high SAR.[54,55] ESI Table 2† demonstrates that PPS-MNPs have shown a higher SAR value than DMSA-MNPs. The SAR and ILP values calculated using eqn (1) and (2) were found to be 245.10 (W g^{-1}) and 2.56 nHm^2 kg^{-1} respectively, which are comparable to or higher than reported values for similar magnetic nanoformulations.[22,56,57] As expected, DMSA-MnFe having a higher M_s value (Fig. 3c and ESI Fig. 4b†) shows a high SAR value compared with other magnetic particles. Similarly, DMSA-CoFe having a high magneto-crystalline anisotropy (H_c) value shows a low SAR value. It is interesting to note that the PPS-MNPs show an almost 1.5 times higher SAR than their corresponding MNPs system. It may be due to possible clustering of individual MNPs into the nanostructured PPS-MNPs core and working synergistically as a single structure to give more high SAR values.[58] Heat-generation phenomena of superparamagnetic PPS-MnFe-NPs in the presence of AMF can be attributed to the Néel and Brownian relaxation.[59] However, PPS-MnFe-NPs with the highest SAR value were selected for the remainder of the studies for hyperthermia applications.

The concentration and time-dependent heating abilities of PPS-MnFe-NPs in the presence of AMF have been studied to check their suitability for hyperthermia application. The time-dependent hyperthermia curves of different concentrations (0.5 to 2 mg mL^{-1}) of PPS-MnFe-NPs dispersion are shown in Fig. 3d. As expected, the heating ability increases with the concentration of the PPS-MnFe-NPs. A concentration of 2 mg mL^{-1} PPS-MnFe-NPs was able to raise the temperature of the solution from 25 to 46 °C in ~27 min, confirming the potential for *in vitro* and *in vivo* hyperthermia applications.

3.9 Drug loading and ROS-responsive release

The drug-loading and release ability of PPS-MnFe NPs were studied using the well-known anticancer drugs DOX and CUR as model drugs. The loading capacity and encapsulation efficiency of DOX in PPS-MnFe NPs calculated using eqn (3) and (4) were found to be 1.2% and 65 ± 3.5%, respectively. The loading capacity and encapsulation efficiency of CUR in PPS-MnFe NPs were found to be 1.6% and 80 ± 3.5%, respectively. The good loading ability of PPS-MnFe NPs can be explained in terms of the excellent hydrophobic interaction between the drug molecules, PPS polymer and hydrophobic MnFe NPs. The release of DOX from PPS-MnFe-DOX NPs in 1× PBS (pH 7.4) at 37 °C temperature is shown in Fig. 4a. In the first 12 h, nearly 16% of DOX release was observed, which reached ~22% at 24 h and remained nearly constant until 72 h of incubation. The minimum release of drug (DOX) in the physiological environment from the PPS-MnFe-DOX NPs is desired for drug delivery application which minimizes the leakage of drug from the particles during storage and blood circulation.[5] The changes in the size of PPS-MnFe NPs under different pH and oxidative conditions were studied to understand the release behaviour of the drug from the respective particle system and are depicted in Fig. 4b. In the presence of low pH and oxidative conditions (H_2O_2), PPS-MnFe NPs showed swelling from 110 nm to 700 nm as shown in Fig. 4b, which may be due to the conversion of the sulphide to sulphone.[36] These data shows that the NPs' size was around 150 nm at normal physiological pH with a narrow PDI (0.193). However, when NPs were incubated in oxidative media at pH 7.4, the NPs swelled and degraded, which is in good agreement with the increase in their size to 250 nm with a PDI > 0.3. CUR-loaded PPS-CUR NPs were developed, and the release profiles recorded in pH 7.4 and acidic pH 5 at 37 °C temperature are shown in Fig. 4c. The release profile of CUR from the PPS-MnFe-CUR NPs in the presence of various stimuli shows that in dual stimuli, *i.e.* low pH and oxidative conditions, nearly 100% drug release was observed within 4 days, compared with only 10% at 6 days of release in the normal physiological conditions (Fig. 4c). On the other hand, in presence of only an oxidative condition at 7.4 pH, release was about 30%. Note that the release of DOX from PPS-MnFe-DOX NPs under ROS/pH stimuli and a cancer-mimicking microenvironment could not be performed as DOX is not stable in oxidative environments, so CUR was used in this study in place of DOX. Additionally, when NPs were exposed to dual stimuli, *i.e.*, low pH and oxidative conditions, the NPs' size changed drastically from 150 nm to 250 nm to eventually 700 nm at 5 mM H_2O_2 and 50 mM H_2O_2, respectively, with PDI > 0.8. Similarly, changes in the particle sizes of PPS-MnFe-CUR NPs were observed (see Fig. SI 5†). These data show that in low pH/oxidative (ROS) conditions, mimicking the tumor microenvironment and lysosomes, different PPS-MNPs showed swelling and degradation resulting in their environment-responsive

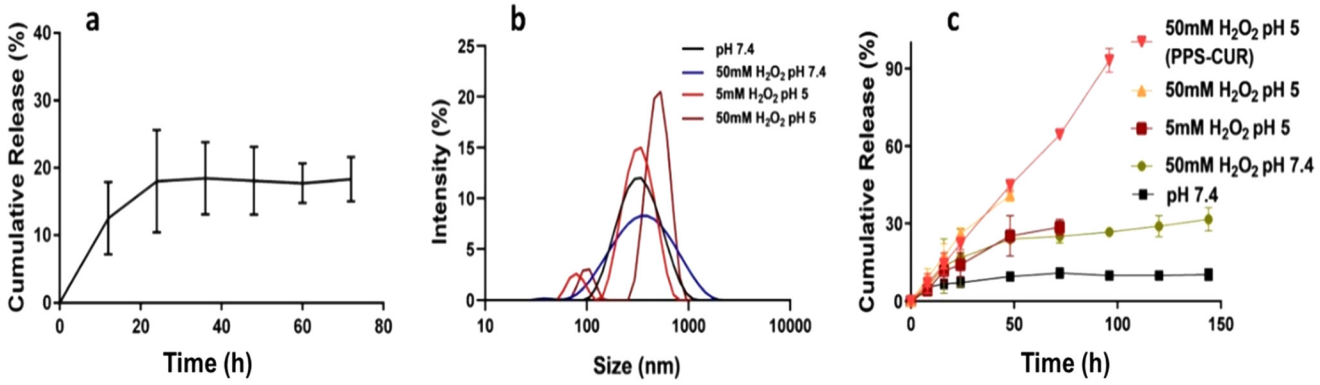

Fig. 4 Release profile of drug and NPs behaviour under various conditions. (a) Release profile data of DOX-loaded PPS-MnFe NPs at 37 °C in 1× PBS (7.4 pH), *i.e.* physiological conditions. This graph shows that in physiological conditions DOX release was in a controlled manner and only 20% release was observed up to 72 h. (b) Gaussian distributions of the hydrodynamic diameter of PPS-MnFe show the effect of different conditions *i.e.* low pH and high ROS or dual stimuli, *i.e.* a combination of ROS and pH, to stimulate the microenvironment of cancer cells. In this graph PPS-MNP shows a drastic increase in size to 700 nm with PDI > 0.8 under dual stimulus conditions compared with the physiological condition where the size is 150 nm. (c) Release profile of CUR from PPS-MnFe-CUR in different conditions *i.e.* low pH and high ROS or dual stimuli, *i.e.* high ROS and low pH. The graph shows that in high ROS and low pH, almost 100% drug was released in 4 days, whereas in the single stimulus (only ROS) condition, the release was 30%, and in physiological conditions, the release was nearly 10%, which demonstrates the dual stimuli-responsive nature of the PPS-MNPs.

drug release, discussed below. The release profiles of drugs from the PPS-MNPs under the stimulus environment (mimicking a tumor) confirm the possibility of site-specific targeted delivery of the drug to reduce the possible side effects and improve the cancer therapeutic efficacy. Note that we have used the UV-vis spectroscopy technique to quantify the DOX in the release as well as encapsulation efficiency study (see method section 2.5.8). However, we also tried to quantify the DOX using its fluorescence spectra; see Fig. SI 6.† However, the possible fluorescence quenching of DOX during several hours of incubation in the release study resulted in inconsistent results. Moreover, magnetic particle interference in the DOX fluorescence was also observed. Thus, we have used nanoparticle digestion method using non-polar solvent, and extracted DOX from the particles to collect only DOX from the digested media as well as release media, followed by spectroscopic determination at 480 nm using an UV-vis spectroscopy method for DOX quantification with negligible interference from components like PPS and MNPs in the quantification.

3.10 ROS-scavenging property of PPS polymer

Metallic NP cytotoxicity is attributed mainly to the generation of high ROS radicals ($HO^{\bullet}$, O_2^- H_2O_2), which cause ROS-mediated lipid, protein, and DNA damage. PPS is a hydrophobic, biodegradable polymer that possesses the property of being converted to its hydrophilic (sulfoxone) form by consuming ROS. PPS is now established to be a well-known anti-inflammatory vehicle mediated *via* its antioxidant nature.[42] The antioxidant property has been tapped recently in inflammatory diseases such as ischemia and periodontal regeneration.[60] We have utilized the PPS coating on the different MNPs (with variable ROS-generating capacity) to quench MNP-mediated ROS production and improve their biocompatibility under *in vitro* and *in vivo* conditions. To evaluate this property, a peroxidase activity assay using TMB substrate in the presence of H_2O_2 was performed and the results are shown in Fig. 5(a–d). In the TMB assay, an interaction of TMB with ROS causes the colourless TMB substrate to oxidise into its blue/green oxidation state.[61] The TMB substrate was incubated with only TMB, PPS NPs, DMSA-MNP and PPS-MNP (M = Fe, MnFe and CoFe) in the presence of hydrogen peroxide (H_2O_2) to check the antioxidant property of PPS in the presence of the MNPs. In Fig. 5(a–d) CoFe has shown an absorbance of 0.6 au (dark blue color) compared with 0.45 au of MnFe and 0.34 au of Fe (light blue color). This result shows that CoFe has more peroxidase-like activity and ROS-generation capacity, followed by MnFe and Fe.[62] However, more than 80% of the TMB radicals were quenched in the presence of the PPS coating on the MNPs compared with DMSA-MNPs, as shown in Fig. 5(a–d). In the pictorial representation, the blue tint that emerged as a result of MNP-mediated ROS reactions with the TMB substrate vanished in the presence of MNPs coated with PPS. A DPPH radical assay was also performed to validate the anti-oxidation property and is shown in Fig. 5e. The assay is based on the measurement of the scavenging capacity of antioxidants towards it. The odd electron of nitrogen atoms in DPPH is reduced by receiving a hydrogen atom from the antioxidants to the corresponding hydrazine.[63] In the presence of PPS, the DPPH radical has been quenched completely and the absorbance peak at 517 nm was reduced significantly; however, there is no effect of MNPs on DPPH radical absorbance. The results show that the antioxidant property of PPS is 94%, which is comparable to 96% of commercial products such as ascorbic acid.

In the *in vitro* setting, the intracellular ROS-scavenging property of PPS was determined by a dichloro-fluorescein dia-

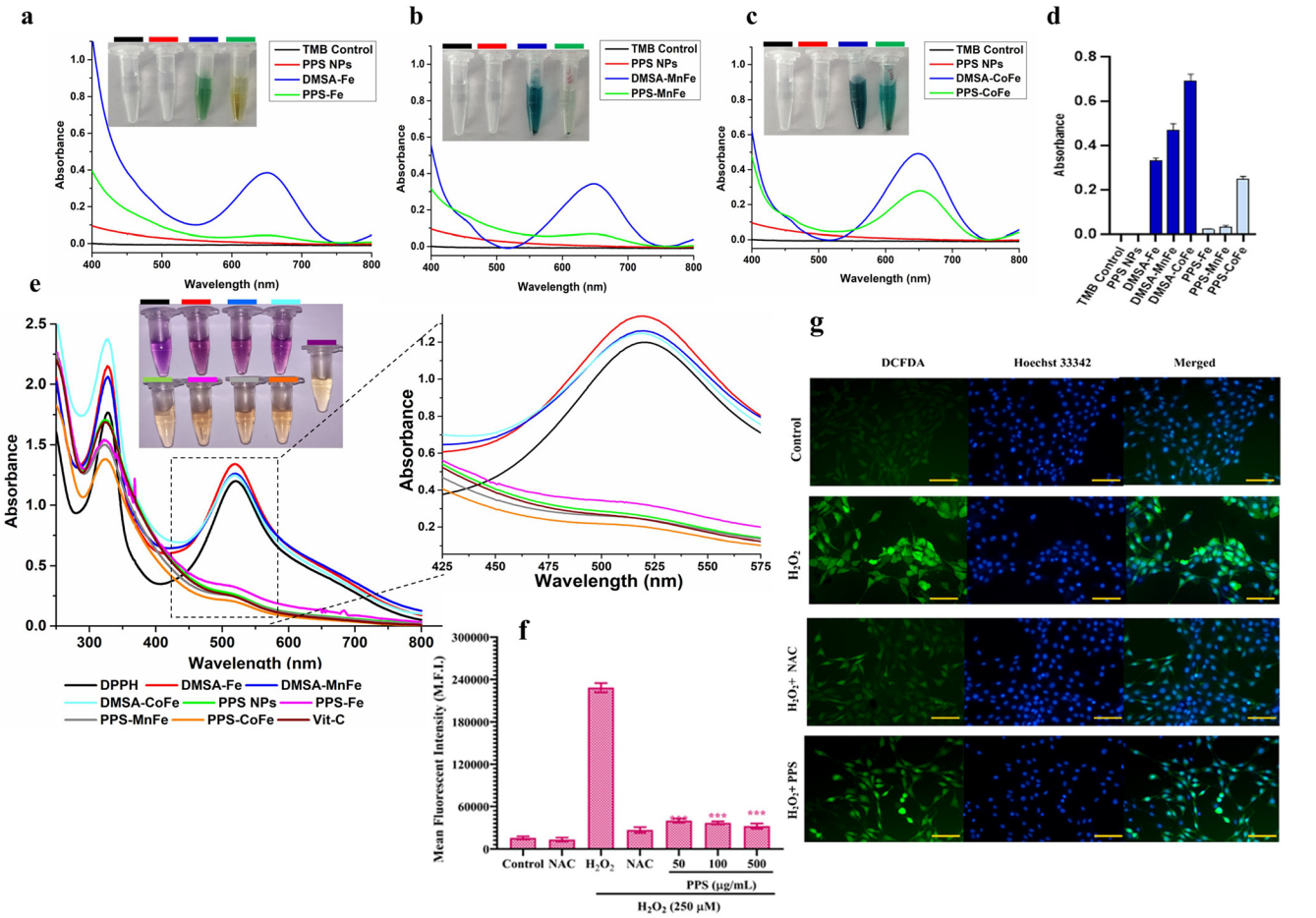

Fig. 5 ROS scavenging property of PPS NPs. (a–c) Quenching of ROS, which are produced by MNPs, with the help of the ROS-scavenging PPS polymer. Here TMB was used as a substrate in the presence of the oxidative inducer H_2O_2 to check the ROS-scavenging property. The green color tube shows more ROS production due to the binding of the radical with TMB. (a) ROS produced by DMSA-Fe NPs (blue line) and quenched in the presence of PPS-Fe (pink line). (b and c) Graphs shown for MnFe and CoFe NPs behavior, respectively. (d) Absorbance measurements of color produced by DMSA-MNPs which produced ROS, compared with PPS-MNPs, where ROS are quenched by the PPS coating. The graph shows that CoFe NPs produced high ROS compared with all other NPs and more than 80% ROS have been quenched by the PPS coating. (e) DPPH radical-based ROS study where MNPs had no effect on the DPPH radical quenching, but PPS-MNPs quenched the 95% DPPH radical, similar to Vit-C (96%). (f) Fluorescence measurements of ROS generated in NIH3T3 cells *via* the DCFDA assay in the presence of the oxidative inducer hydrogen peroxide and scavenging by different concentrations of PPS NPs. (g) Fluorescence microscopic observation of ROS generation evaluated by DCFDA substrate in NIH3T3 cells treated with hydrogen peroxide and antioxidant (conventional *N*-acetyl cysteine and PPS NPs). Scale bar: 25 μm.

cetate (DCFDA) assay as shown in Fig. 5(f and g). The cells were first treated with varying concentrations of PPS NPs, allowed sufficient time (12 h) for uptake and treated with the exogenous ROS-generating agent H_2O_2 to generate intracellular ROS. DCFDA was added to determine the ROS generation and scavenging property of H_2O_2 and PPS NPs respectively. As shown in Fig. 5f, negligible fluorescence could be detected from both the control group and the PPS NPs-treated groups along the concentration gradient. However, a high fluorescence signal was detected in the H_2O_2 group, which demonstrated that the intracellular non-fluorescent DCFDA could be oxidized by ROS to generate the fluorescent 2,7-dichlorofluorescein (DCF). With the assistance of PPS NPs, the fluorescence intensity from the H_2O_2-treated group decreased significantly. The results indicate nearly 80% ROS could be removed by PPS NPs upon co-incubation of cells at a concentration of 50 μg mL^{-1} and above. For comparison, *N*-acetyl cysteine (NAC), as an endogenous antioxidant against ROS was used in this study. As shown in Fig. 5f, PPS NPs with concentrations of 50 μg mL^{-1} and above held a similar ROS removal capacity with that of NAC with a concentration of 5 mM.

These results were also confirmed by fluorescence microscopy (Fig. 5g). Untreated cells showed minimal levels of intracellular ROS (almost undetectable levels of fluorescence), whereas the intense ROS signal of H_2O_2-treated cells was strongly attenuated by PPS-NPs comparable to that of NAC. Collectively, our *in vitro* results demonstrate that PPS-NPs display a high-performance ROS-scavenging property outside and inside cells as hypothesized, which is beneficial for the biocompatibility of different magnetic particles (discussed

below) and for enabling tumor/inflammation microenvironment (ROS) mediated drug release towards cancer or other disease conditions. In this study we have used ROS by a PPS-nanocarrier system for dual purposes, namely (a) the tumor microenvironment-responsive release of drugs as well as (b) to improve the biocompatibility of magnetic particles.

3.11 Cellular uptake

Efficient internalization of particles is essential for any nanocarrier for drug delivery application. The *in vitro* uptake of MNPs (*i.e.*, intracellular Fe ions) was confirmed *via* the Prussian blue staining method, flow cytometry and fluorescence microscopy. It can be noted from the Prussian blue staining microscopic images in Fig. 6a that the control cells have not displayed any blue staining. Moreover, the cells have displayed the blue staining when they are incubated with bare (DMSA-MnFe) and PPS-MnFe particles at the indicated concentration of 50 μg mL^{-1}. This indicates that the MNPs are effectively taken up by the MCF7 cells at 6 h of incubation.

We also performed a quantitative uptake of PPS-DOX particles in a time-dependent manner by flow cytometry as shown in Fig. 6b. The results indicate effective cellular uptake at 0.5, 1 and 3 h. Since DOX is a fluorescent moiety, we used the auto-fluorescence property of DOX to visualize the internalization of PPS-MnFe-DOX into MCF-7 cancer cells. As shown in Fig. 6c, the cells exhibited fluorescence after 3 h of incubation when compared with the control. Therefore, we can conclude that the PPS-MnFe and PPS-MnFe-DOX particles are efficiently taken up by the cells and therefore their use for *in vitro* MHT could be used for cancer thermal therapies. It is confirmed from the above result including the *in vitro* ROS-quenching study, that the PPS and PPS-MNPs show high internalization into the cells.

3.12 Biocompatibility of different MNPs and PPS-coated MNPs

The biocompatibility of metallic NPs is a crucial consideration before putting them to use in biological applications. As discussed before, the intrinsic toxicity and poor aqueous stability of metallic NPs, particularly magnetic NPs, prevents their widespread application in different biomedical applications including cancer theranostics.[28] Oxidative stress is assumed to be the primary source of MNP toxicity at the cellular level.[12] An increase in apoptosis and poor cell metabolism can result from the release of ROS from MNPs, as well as from the release of metal ions from the core, or from the release of oxidants through enzymatic destruction. To circumvent the limit-

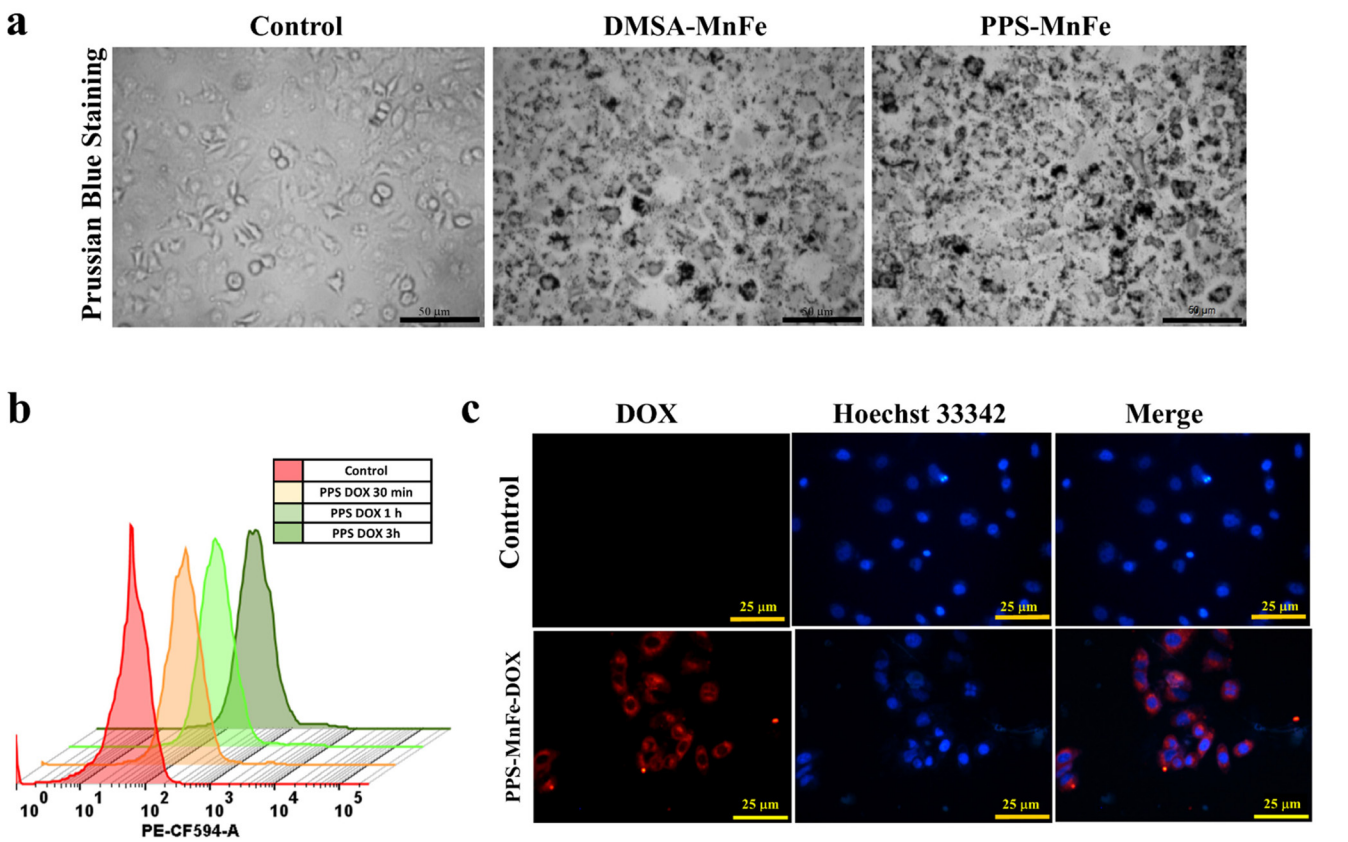

Fig. 6 Intracellular uptake of PPS MNPs. (a) Prussian blue staining of MNP uptake by breast cancer MCF-7 cells after 6 h. Control denotes no addition of particles, DMSA-MnFe denotes uptake of magnetic MnFe particles coated with DMSA and PPS-MnFe denotes particle uptake of PPS-coated MnFe NPs. (b) Time-lapse (0, 0.5, 1, and 3 h) uptake of PPS NPs loaded with doxorubicin into MCF-7 cells, acquired by flow cytometry (c). Fluorescence microscopic images of the intracellular uptake of PPS-MnFe-DOX NPs into MCF-7 cells after 3 h. Scale bar: (a) 50 μm, (c) 25 μm.

ations, we hypothesized that an appropriate polymer coating with ROS-scavenging capabilities, such as PPS, can be used to drastically improve the biocompatibility of magnetic as well as similar metallic NPs.

In this regard, the comparison of cellular viability with different MNPs (DMSA-Fe/MnFe/CoFe) and PPS-coated formulations of Fe/MnFe/CoFe was determined using two cells, murine fibroblast NIH3T3 cells and human embryonic kidney HEK293 cells, treated with varying concentrations (100–1000 μg mL^{-1}) of the NPs. The cellular viability test (MTS test) confirmed that, in the concentrations used for the assays, the PPS-MNP system shows enhanced biocompatibility compared with non-coated magnetic NPs. The results presented in Fig. 7 indicate that there is a significant difference in the cytotoxicity between bare (DMSA-coated) and PPS-coated magnetic particles. As shown in Fig. 7 and SI 7,† the PPS-coated particles exhibited 2–3 fold more biocompatibility than their bare counterparts, determined from their IC_{50} concentration at 24, 48 and 72 h, indicating their protective and excellent biocompatible nature. As a measure of their IC_{50} values, it is observed that the bare DMSA-Fe particles impart toxicity at around 250 μg mL^{-1} after 72 h of incubation whereas their PPS counterpart exhibits toxicity at around 674 μg mL^{-1} at the same time interval (Fig. 7a). Similarly, the improvement in biocompatibility was observed for the MnFe and CoFe particle systems. DMSA-MnFe exhibits an IC_{50} around 210 μg mL^{-1} and PPS-MnFe shows toxicity around 580 μg mL^{-1} at 72 h post incubation with the particles (Fig. 7b). The PPS-CoFe system exhibited twice the biocompatibility as demonstrated by the IC_{50} value of DMSA-CoFe (194 μg mL^{-1}) and PPS-CoFe (412 μg mL^{-1}) at 72 h (Fig. 7c). A similar outcome was achieved when the same was performed on a different cell line, HEK293 cells, using the similar experimental plan. As shown in Fig. SI 7,† the PPS-coated MNPs exhibited a similar improvement in their cellular viability as compared with their DMSA counterparts. On an average, an improvement of 2–3 times in cellular viability was observed and consistent over the two cell lines. The IC_{50} values for DMSA-MNPs are concordant with previous reports demonstrating that the toxicity of magnetic particles follow the order as obtained by us, *i.e.* Fe < MnFe < CoFe.[9] The biocompatible nature of the delivery system itself (*i.e.* plain PPS) was studied and is shown in Fig. SI 8.† The system shows excellent biocompatibility in both cell lines up to 2 mg mL^{-1} concentrations when treated for 24, 48 and 72 h. We also assessed the morphology of the cells at two selected concentrations (100 and 250 μg mL^{-1}) of DMSA-MnFe and PPS-MnFe after 72 h to reveal the biocompatible nature of the coating. Fig. SI 9 and SI 10† depict the brightfield microscopic images

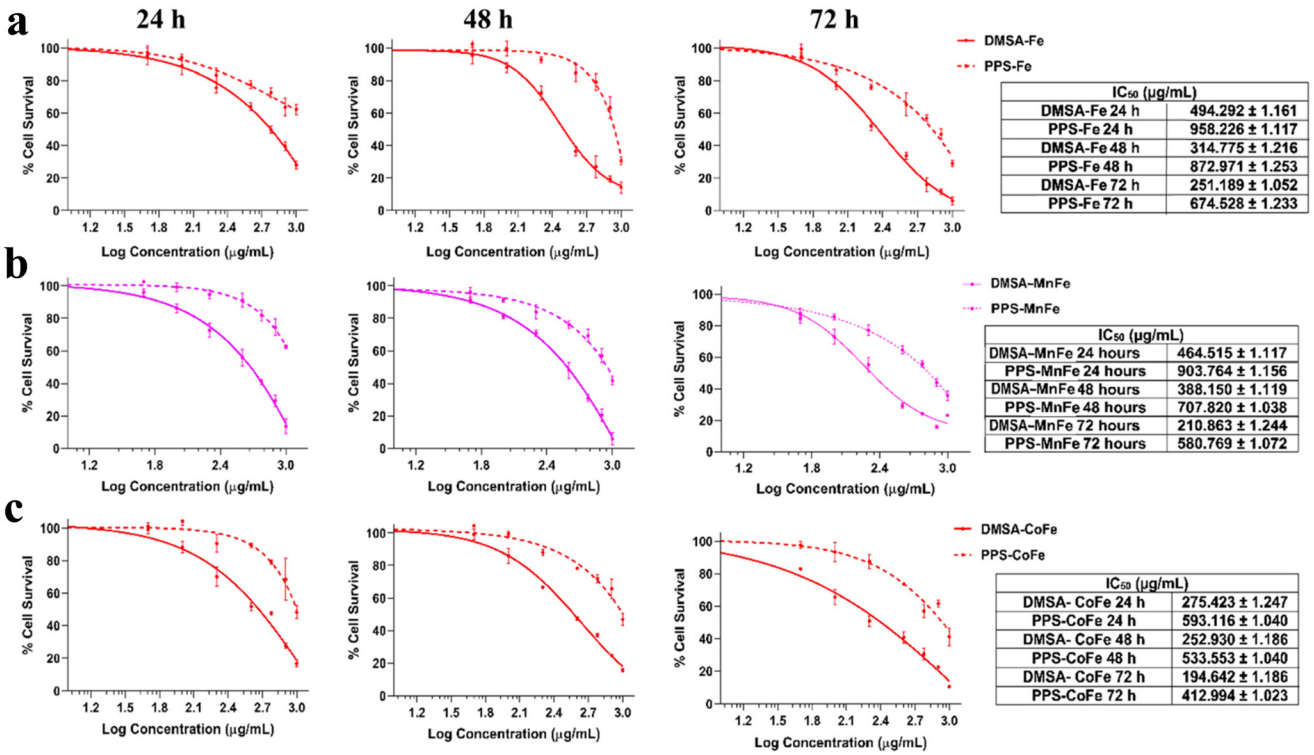

Fig. 7 PPS coating enhances the biocompatibility of various magnetic NPs. (a) Cell viability assessment by MTS assay of NIH3T3 cells with DMSA-Fe NPs (solid line) and PPS-Fe NPs (dashed line) with variable concentrations (0–1000 μg mL^{-1}) for 24, 48 and 72 h incubation along with the IC_{50} values. (b) Cell viability assessment by MTS assay of NIH3T3 cells with DMSA-MnFe NPs (solid line) and PPS-MnFe NPs (dashed line) with variable concentrations (0–1000 μg mL^{-1}) for 24, 48 and 72 h incubation along with the IC_{50} values. (c) Cell viability assessment by MTS assay of NIH3T3 cells with DMSA-CoFe NPs (solid line) and PPS-CoFe NPs (dashed line) with variable concentrations (0–1000 μg mL^{-1}) for 24, 48 and 72 h incubation along with the IC_{50} values.

of NIH3T3 and HEK293 cells respectively, after treatment, which show the gross cellular changes observed with bare particles, whereas the PPS-coated particles maintain their morphology to a great extent.

We validated our hypothesis with three different particle systems, namely Fe, MnFe and CoFe, where we have observed varying cytotoxicity (CoFe > MnFe > Fe) of the different magnetic particles ascribed to their ROS-generation capacity, as reported in the literature[22] as well as shown in our *in vitro* ROS activity experiments (Fig. 5a–e). PPS particles as a ROS-scavenging moiety confer the nanosystem with the advantage of being a safe system and in the tumor milieu can act as a double edged sword to act as a dual stimuli-responsive nanocarrier. Bare MNPs exert significant cytotoxicity *in vitro* as well as *in vivo*.[64] In order to improve the biocompatibility, various coatings and functionalization such as dextran, silica, PEG, tannic acid, *etc*. have been employed but with limited success.[65–68] To our knowledge, our approach can increase biocompatibility up to three times than the bare MNPs over long periods of time (72 h). The results are consistent with the *in vitro* ROS-scavenging capability (Fig. 5a–d) of the coated MNPs, demonstrating their biocompatibility for cancer theranostic applications, and offer great potential for the application of PPS as a nano-delivery method. Such systems show great potential for enhancing the toxicity and stability of not just magnetic NPs, but also other types of metallic NPs, allowing one to leverage the many properties of metallic NPs without sacrificing their toxicity.

3.13 *In vitro* chemotherapy and dual thermo-chemotherapy

The application of our PPS-MNP system was further used to check their cancer therapeutic application as a most promising model application. Our developed nanoplatform (*i.e.* PPS MnFe-DOX) was evaluated for its *in vitro* anticancer cytotoxic potential. We studied their effects on breast adenocarcinoma cells (MCF-7) in a dose (0–200 μg mL^{-1}) and time (48 and 72 h) dependent manner. As shown in Fig. 8a and Fig. SI 11,† DOX-loaded PPS-MnFe particles are more toxic than the equivalent DOX alone (0–2.75 μg mL^{-1}) and only PPS-MnFe particles, the results being statistically significant. In all cases, the plain PPS particles demonstrated low toxicity with >75% cellular viability at the highest concentration after 72 h in MCF-7 cells.

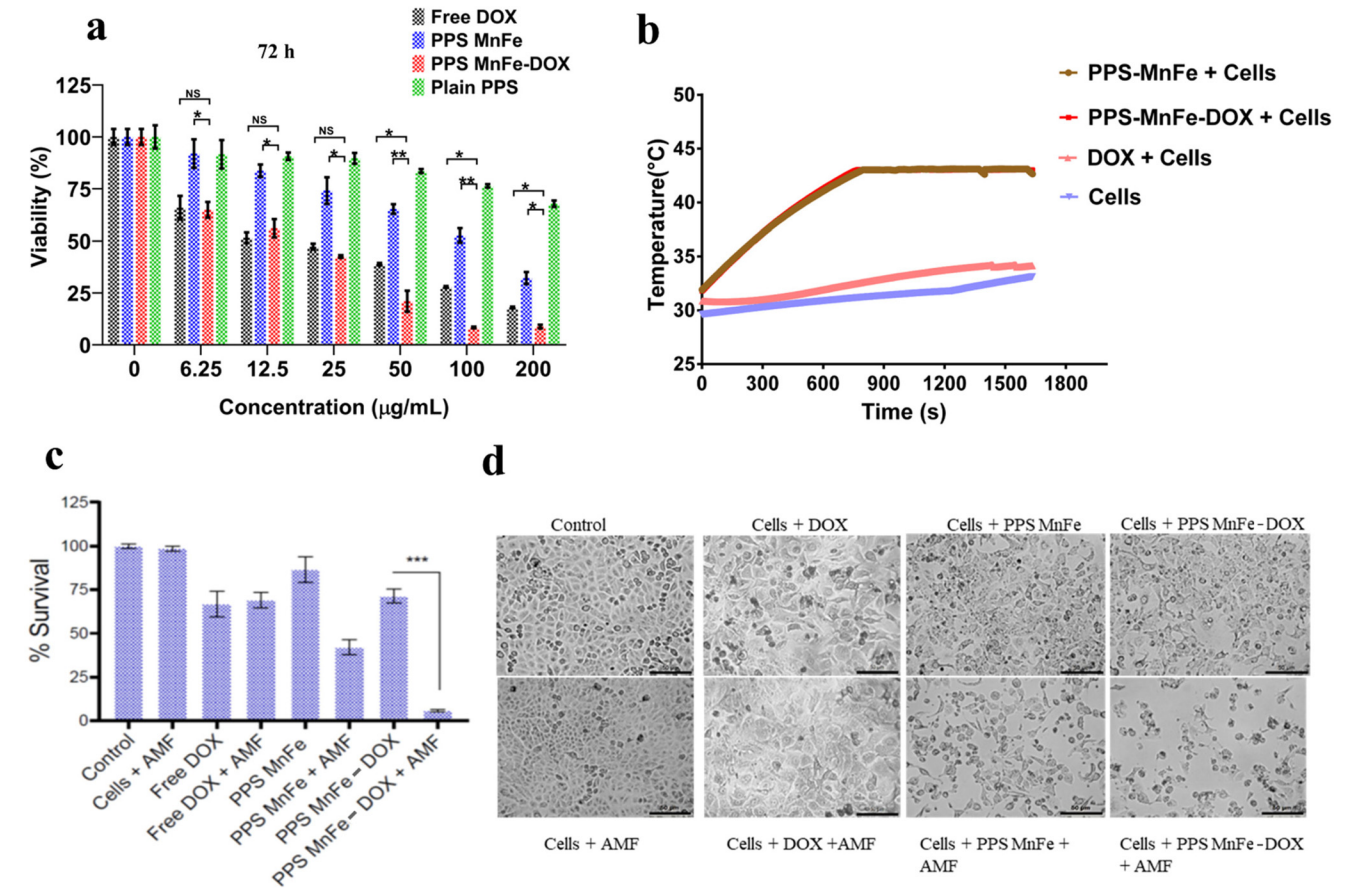

Fig. 8 MNPs induce a synergistic effect of hyperthermia and chemotoxicity on breast cancer cells. (a) Assessment of the cellular toxicity of free DOX, PPS-MnFe, PPS-MnFe-DOX and blank PPS NPs on MCF-7 cells after 72 h of treatment by MTS assay. (b) Time course of the temperature rise of culture solution containing cells (no NPs), free DOX + cells, PPS-MnFe + cells, PPS-MnFe-DOX + cells while attaining a therapeutic temperature. (c) Cellular toxicity induced by free DOX, PPS-MnFe and PPS-MnFe-DOX in the presence and absence of AMF assessed by MTS assay. (d) Brightfield microscopic images of MCF-7 cells acquired after subjecting them to dual chemo-hyperthermia treatment, after 24 h. Scale bar: 50 μm.

The treatment of cancer is a multi-step process. Utilizing more than one drug or therapy method simultaneously allows for the simultaneous targeting of many mechanisms in the progression of a tumour. The heterogeneity of the tumour is a significant contributor to the unsatisfactory performance of single treatment modules. Combination therapy, as opposed to single therapy, consequently provides a number of benefits. Combining several types of chemotherapy, or chemotherapy with other modalities such as hyperthermia or immunotherapy, is one way to improve the odds that the disease will be completely eradicated. We therefore evaluated the dual modality of cell-killing by chemo- and thermo-mediated cytotoxicity. To perform chemo-thermo-mediated treatment, cancer cells were treated with MnFe, PPS-MnFe and DOX in the presence of an alternating magnetic field (AMF) in a nanotherm instrument to achieve a therapeutic temperature of 45 °C as shown in Fig. 8b. To attain the desired temperature (45 °C), MNPs and PPS-MNPs took around 12 min (750 s) and the temperature was maintained around 45 °C for the next 15 min. However, with DOX samples and only-cells samples, the temperature remained the same (32 °C) upon exposure to AMF.

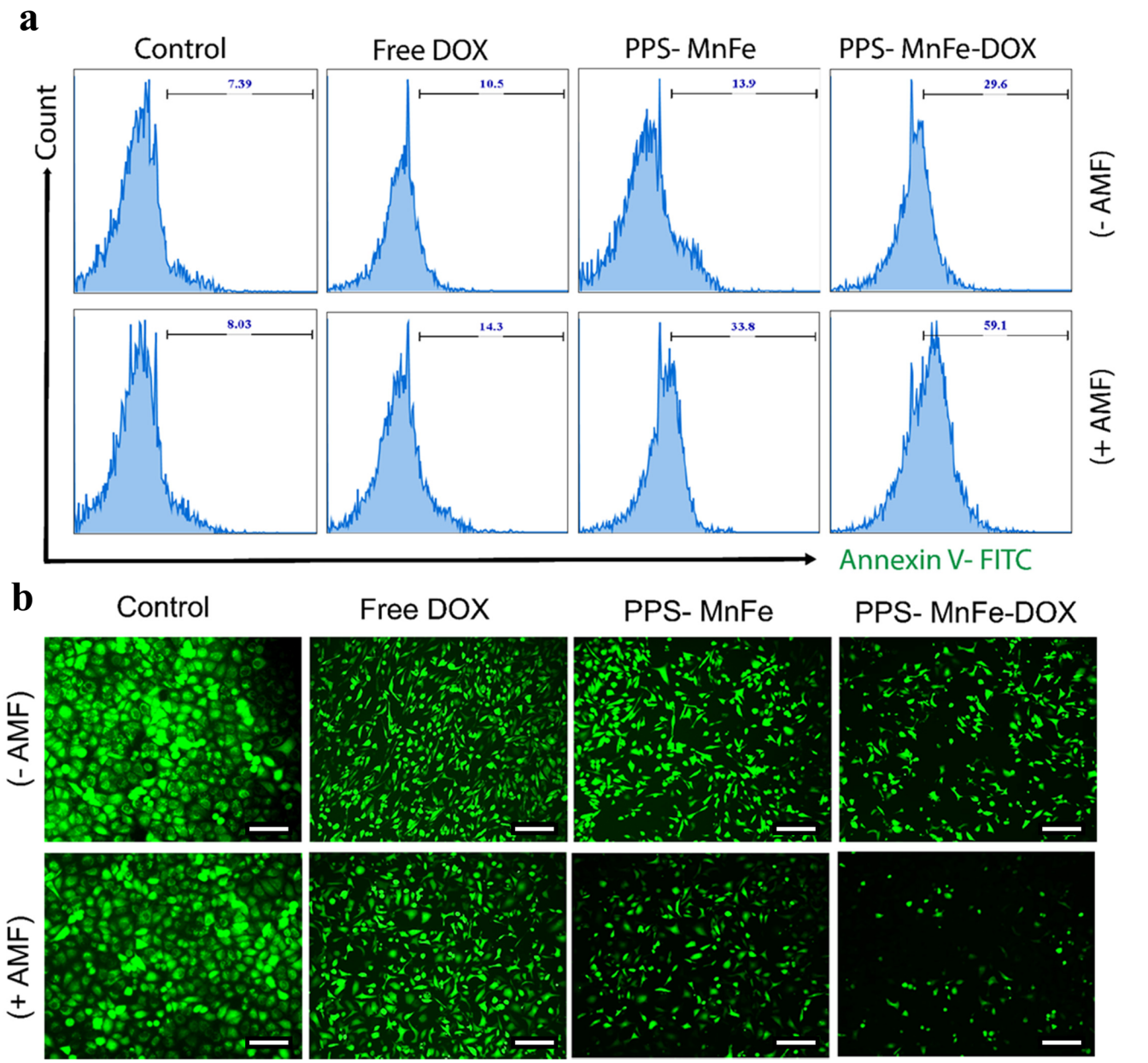

Fig. 9 Mechanistic study of magnetic NPs to eliminate breast cancer cells by dual thermo-chemotherapy. (a) Doxorubicin (DOX)-loaded PPS-MnFe NPs induced apoptosis in MCF-7 cells. Cells were treated separately with free DOX, PPS-MnFe, and PPS-MnFe-DOX with and without MHT. Apoptotic cell death was detected by staining the cells with an Annexin-V kit and analyzed by flow cytometry. (b) Fluorescence images of MCF-7 cells stained with 2 μM calcein-AM after chemo-hyperthermia therapy alone as well as combined after 24 h. The green signal signifies emission from calcein-AM, indicating live cells. Scale bar: 50 μm.

DOX is a drug that has been approved by the FDA to treat cancer. It works by creating DNA lesions in the cancer cells thereby leading to cell death. However, the drug has unwanted side effects and cancer cells can become resistant to it over time. MHT on the other hand works by inducing damage to the cell machinery upon exposure to heat. So, in our study, adding a different way to kill cells, like MHT, helped DOX to kill breast cancer cells in a much more effective way. We aimed to target two different modes of cell killing to achieve the maximum response from dual therapy. Therefore, the anticancer effects of PPS-MnFe-DOX in response to AMF were investigated on MCF7 cells in three scenarios: hyperthermia alone (45 °C), chemotherapy alone (DOX 2.75 μg mL^{-1}), and combined therapy for 15 min. No considerable changes were observed in the MCF7 cells treated with only AMF as compared with the controls, as shown in Fig. 8c. However, the MCF7 cells that were treated with 2 mg mL^{-1} bare PPS-MnFe (without exposing to AMF), corresponding to an equivalent drug concentration of 2.75 μg mL^{-1}, exhibited a lower cell death percentage and fewer morphological changes are observed. But after MHT treatment, the drug-loaded and bare PPS-MnFe induced ~95 and ~55% cell death at 2 mg mL^{-1} concentration, respectively (Fig. 8c) and considerable morphological changes were observed as indicated in Fig. 8d. The enhanced anticancer efficacy of PPS-MnFe-DOX compared with MnFe alone may be ascribed to better heating responses under the applied AMF, as discussed in previous sections. The short treatment duration may also help in reducing unwarranted heat-mediated bystander cell killing in an *in vivo* setting. It is interesting to note that the generation of ROS within the cells is one of the killing means among various agents/mechanisms of the cancer cells during chemo/thermo-chemotherapy. Although the PPS-MnFe-DOX consumed some fraction of cellular ROS for the responsive release of DOX, however, the DOX-mediated cancer cell killing efficacy using PPS-MnFe-DOX or free DOX is not affected (see Fig. 8, free DOX and PPS-MnFe-DOX). Similarly, we observed effective cancer cell killing from the combined thermo-(hyperthermia)-chemotherapy (DOX) using our PPS-MNP-DOX system. It is attributed to a possible, relatively smaller fraction of ROS consumed by the PPS-nanocarrier without a significant change in the ROS concentration within the cells, or/and other means of killing of cancer cells except for ROS-mediated ones are more prominent for DOX as well as hyperthermia or their combination.[59,69]

3.14 Mechanism of cancer cell death under dual chemo-hyperthermia

To further assess the effect of thermo- and chemotherapy on the breast cancer cells, the cells treated with chemotherapy and hyperthermia and a combination were stained with annexin V. Annexin V is a well-established marker to quantify the onset of apoptosis.[70] As shown in Fig. 9a, the fraction of apoptotic cells was highest (59.1%) in the combined therapy module on application of AMF, while the number for the control groups was around 7–8%, and for the free DOX-treated samples was around 10.5% without AMF and 14.3% with AMF, followed by PPS-MnFe-treated samples with 13.9% apoptotic cells in the non-AMF group, which escalated to 33.8% with AMF. The results are expected and in accordance with the cell viability data, indicating that the combined therapy is more efficacious than the single-therapy module.

In addition, the cells after treatment with MHT were subjected to live cell estimation. As DOX is used in the chemotherapy module, its inherent fluorescence would interfere with the fluorescent signals of propidium iodide or 7-AAD, and hence, only live cell estimation was carried out. As shown in Fig. 9b, the control cells emitted an intense green colour attributed to calcein AM fluorescence in live cells only. The intensity is seen to decline/fade in other treatment groups with the combined treatment group in the presence of AMF, showing the least number of viable (green) cells. The results collectively demonstrate that the magnetic nanoplatform effectively induces cell death *via* apoptosis and proffers an excellent system for future *in vivo* theranostics applications.

4. Conclusion

Magnetic nanodelivery systems comprising superparamagnetic nanoparticles of Fe_3O_4 (Fe), $MnFe_2O_4$ (MnFe), $CoFe_2O_4$ (CoFe), and $NiFe_2O_4$ (NiFe) are most promising for magnetic drug targeting, MRI contrast agents, hyperthermia and other biomedical applications. However, several limitations related to magnetic nanocarriers such as loading of drugs, targeted tumor accumulation, *in vivo* degradation, and oxidative stress-mediated (ROS) toxicity remain yet to be addressed. Coating/functionalization by biodegradable polymers or molecules to reduce the toxicity has limited outcome as this coating degradation finally leads the magnetic particle's matrix to be exposed to the biological environment and subsequent ROS-mediated toxicity. Our novel approach of a ROS-scavenging polymer (PPS) coating on MNPs (PPS-Fe, PPS-MnFe and PPS-CoFe) endowed the MNPs with biocompatibility three times greater than that of bare MNPs, high drug loading (2.6% loading capacity) and dual stimuli-responsive (pH and ROS, tumor microenvironment) drug release magnetic carriers for combination therapy, hyperthermia and chemotherapy. Here, different MNPs (Fe/MnFe/CoFe) with variable ROS-generating potential with DMSA or PPS coating were synthesized and their physicochemical properties, toxicity, and heating capacity under AMF hyperthermia were thoroughly investigated for combined therapy application in *in vitro* settings. PPS coating on these magnetic particles not only provides synchronized degradation of the PPS polymer along with magnetic particles in the lysosomal compartment, but also constant scavenging of ROS generated from the degrading MNPs, thus reducing the oxidative stress and toxicity of the MNPs. While screening the MNPs for their heating ability, bare and coated MNPs exhibited excellent heating capacity with DMSA-MnFe and PPS-MnFe NPs exhibiting the highest SAR values, *i.e.* 245 and 214 W g^{-1} respectively, reaching the therapeutic temperature window of 37 to 42 °C within 10 min. Similarly, PPS-DOX-MNPs/

PPS-CUR-MNPs show 100% release of drug under dual stimulation conditions, ROS and pH < 6 (mimicking the tumor microenvironment pH range from 5–7) in 4 days compared with approximately 10% in the normal physiological condition (pH 7.4), confirming the possible targeted delivery of the drug to the tumor site (or disease condition). Similarly, one can expect to add magnetic targeting along with target-specific release to enhance the targeted delivery of magnetic nanocarriers for better therapeutic efficacy and minimal side effects.

Though here we have reported the PPS-coated-drug and MNP system for one of the possible applications of cancer therapeutics using combined chemo- and hyperthermia as an example, this novel magnetic nano-delivery system could be used for MRI imaging for diagnostic and other therapeutic applications where the targeted delivery could be achieved by dual targeting, or magnetic-field-mediated and disease-specific microenvironment (pH and ROS) responsive release. In this study, we have investigated and validated our hypothesis in the *in vitro* condition which needs further authentication in the *in vivo* model, and is under process. Our approach of a ROS-responsive polymer, PPS coating to address several challenges (toxicity, high drug loading, targeted delivery and degradation) related to smart magnetic nanocarrier development for clinical use, is a generic yet novel one-for-all solution which can be easily adaptable to any other metallic or metal oxide NP system, contributing to toxicity from the oxidative stress and other disease conditions with a high inflammatory index. To the best of our knowledge, we are the first to report such a novel generic approach to overcome several challenges to make magnetic-nano carriers for biomedical applications.

Conflicts of interest

The authors declare that they do not have any conflict of interest.

Acknowledgements

The authors are thankful to the TEM facility at the Indian Institute of Technology, Hyderabad for TEM imaging of samples. We are also thankful to Department of Biotechnology (DBT Project numbers- (BT/PR14629/NNT/28/823/2015) (BT/RLF/Re-entry/2013), Department of Science and Technology (DST) (Project Numbers- DST/IMRCD/EU/INNO-INDIGO/NANOBREASTCO/2015 and IMP/2018/000687).

References

1 V. F. Cardoso, A. Francesko, C. Ribeiro, M. Bañobre-López, P. Martins and S. Lanceros-Mendez, *Adv. Healthcare Mater.*, 2018, **7**, 1700845.
2 X. Li, J. Wei, K. E. Aifantis, Y. Fan, Q. Feng, F.-Z. Cui and F. Watari, *J. Biomed. Mater. Res., Part A*, 2016, **104**, 1285–1296.
3 W. Wu, C. Z. Jiang and V. A. L. Roy, *Nanoscale*, 2016, **8**, 19421–19474.
4 T. Neuberger, B. Schöpf, H. Hofmann, M. Hofmann and B. von Rechenberg, *J. Magn. Magn. Mater.*, 2005, **293**, 483–496.
5 D. Bobo, K. J. Robinson, J. Islam, K. J. Thurecht and S. R. Corrie, *Pharm. Res.*, 2016, **33**, 2373–2387.
6 Y.-X. J. Wang, *World J. Gastroenterol.*, 2015, **21**, 13400–13402.
7 H. Du, O. U. Akakuru, C. Yao, F. Yang and A. Wu, *Transl. Oncol.*, 2022, **15**, 101264.
8 M. Abudayyak, T. AltinçekİÇ Gürkaynak and G. Özhan, *Turk. J. Pharm. Sci.*, 2017, **14**, 169–173.
9 H. Zhao, Z. Chen, L. Tao, X. Zhu, M. Lan and Z. Li, *RSC Adv.*, 2015, **5**, 68454–68460.
10 M. Bellusci, A. La Barbera, F. Padella, M. Mancuso, A. Pasquo, M. G. Grollino, G. Leter, E. Nardi, C. Cremisini, P. Giardullo and F. Pacchierotti, *Int. J. Nanomed.*, 2014, **9**, 1919–1929.
11 Z. Yu, Q. Li, J. Wang, Y. Yu, Y. Wang, Q. Zhou and P. Li, *Nanoscale Res. Lett.*, 2020, **15**, 115.
12 R. J. Wydra, P. G. Rychahou, B. M. Evers, K. W. Anderson, T. D. Dziubla and J. Z. Hilt, *Acta Biomater.*, 2015, **25**, 284–290.
13 R. J. Wydra, C. E. Oliver, K. W. Anderson, T. D. Dziubla and J. Z. Hilt, *RSC Adv.*, 2015, **5**, 18888–18893.
14 Q. Feng, Y. Liu, J. Huang, K. Chen, J. Huang and K. Xiao, *Sci. Rep.*, 2018, **8**, 2082.
15 D. B. Cochran, P. P. Wattamwar, R. Wydra, J. Z. Hilt, K. W. Anderson, R. E. Eitel and T. D. Dziubla, *Biomaterials*, 2013, **34**, 9615–9622.
16 A. K. Gupta and A. S. G. Curtis, *J. Mater. Sci. Mater. Med.*, 2004, **15**, 493–496.
17 H. Xu, L. Cui, N. Tong and H. Gu, *J. Am. Chem. Soc.*, 2006, **128**, 15582–15583.
18 C. C. Berry, S. Wells, S. Charles, G. Aitchison and A. S. G. Curtis, *Biomaterials*, 2004, **25**, 5405–5413.
19 H. Nosrati, M. Salehiabar, S. Davaran, A. Ramazani, H. K. Manjili and H. Danafar, *Res. Chem. Intermed.*, 2017, **43**, 7423–7442.
20 H. H. Gustafson, D. Holt-Casper, D. W. Grainger and H. Ghandehari, *Nano Today*, 2015, **10**, 487–510.
21 R. M. Patil, N. D. Thorat, P. B. Shete, P. A. Bedge, S. Gavde, M. G. Joshi, S. A. M. Tofail and R. A. Bohara, *Biochem. Biophys. Rep.*, 2018, **13**, 63–72.
22 P. Pradhan, J. Giri, G. Samanta, H. D. Sarma, K. P. Mishra, J. Bellare, R. Banerjee and D. Bahadur, *J. Biomed. Mater. Res., Part B*, 2007, **81**, 12–22.
23 T. Mai and J. Z. Hilt, *Colloids Surf., A*, 2019, **576**, 9–14.
24 M. O. Ansari, N. Parveen, M. F. Ahmad, A. L. Wani, S. Afrin, Y. Rahman, S. Jameel, Y. A. Khan, H. R. Siddique, M. Tabish and G. G. H. A. Shadab, *Sci. Rep.*, 2019, **9**, 6912.
25 A. J. Gauger, K. K. Hershberger and L. M. Bronstein, *Front. Chem.*, 2020, **8**, 561.
26 C. Zhang, D. Li, P. Pei, W. Wang, B. Chen, Z. Chu, Z. Zha, X. Yang, J. Wang and H. Qian, *Biomaterials*, 2020, **237**, 119835.
27 A. L. B. Seynhaeve, M. Amin, D. Haemmerich, G. C. van Rhoon and T. L. M. ten Hagen, *Adv. Drug Delivery Rev.*, 2020, **163–164**, 125–144.

28 N. R. Datta, S. Krishnan, D. E. Speiser, E. Neufeld, N. Kuster, S. Bodis and H. Hofmann, *Cancer Treat. Rev.*, 2016, **50**, 217–227.
29 J. Du, L. A. Lane and S. Nie, *J. Controlled Release*, 2015, **219**, 205–214.
30 G. Waris and H. Ahsan, *J. Carcinog.*, 2006, **5**, 14.
31 B. Chen, C. Zhang, W. Wang, Z. Chu, Z. Zha, X. He, W. Zhou, T. Liu, H. Wang and H. Qian, *ACS Nano*, 2020, **14**, 14919–14928.
32 K. Poole, C. Nelson, R. Joshi, J. Martin, M. Gupta, S. Haws, T. Kavanaugh, M. Skala and C. Duvall, *Biomaterials*, 2015, **41**, 166–175.
33 Z. Li, Z. Chu, J. Yang, H. Qian, J. Xu, B. Chen, T. Tian, H. Chen, Y. Xu and F. Wang, *ACS Nano*, 2022, **16**, 15471–15483.
34 J. Liu, Y. Li, S. Chen, Y. Lin, H. Lai, B. Chen and T. Chen, *Front. Chem.*, 2020, **8**, 838.
35 A. Rehor, J. A. Hubbell and N. Tirelli, *Langmuir*, 2005, **21**, 411–417.
36 M. Chauhan, S. M. Basu, S. K. Yadava, N. Sarviya and J. Giri, *J. Appl. Polym. Sci.*, 2022, **139**, 51767.
37 S. Sun and H. Zeng, *J. Am. Chem. Soc.*, 2002, **124**, 8204–8205.
38 L. D. Bianco, F. Spizzo, G. Barucca, M. R. Ruggiero, S. G. Crich, M. Forzan, E. Sieni and P. Sgarbossa, *Nanoscale*, 2019, **11**, 10896–10910.
39 Z. P. Chen, Y. Zhang, S. Zhang, J. G. Xia, J. W. Liu, K. Xu and N. Gu, *Colloids Surf., A*, 2008, **316**, 210–216.
40 D. Kaushik and G. Bansal, *J. Pharm. Anal.*, 2015, **5**, 285–295.
41 S. K. Yadava, S. M. Basu, R. Valsalakumari, M. Chauhan, M. Singhania and J. Giri, *ACS Appl. Bio Mater.*, 2020, **3**, 6811–6822.
42 K. M. Poole, C. E. Nelson, R. V. Joshi, J. R. Martin, M. K. Gupta, S. C. Haws, T. E. Kavanaugh, M. C. Skala and C. L. Duvall, *Biomaterials*, 2015, **41**, 166–175.
43 S. M. Basu, S. K. Yadava, R. Singh and J. Giri, *Colloids Surf., B*, 2021, **204**, 111775.
44 J. Lim, S. P. Yeap, H. X. Che and S. C. Low, *Nanoscale Res. Lett.*, 2013, **8**, 381.
45 P. M. Price, W. E. Mahmoud, A. A. Al-Ghamdi and L. M. Bronstein, *Front. Chem.*, 2018, **6**, 619.
46 K. H. Bae, S. H. Choi, S. Y. Park, Y. Lee and T. G. Park, *Langmuir*, 2006, **22**, 6380–6384.
47 Q. Yu, L. Zhao, C. Guo, B. Yan and G. Su, *Front. Bioeng. Biotechnol.*, 2020, **8**, 210.
48 J. Mohapatra, S. Nigam, J. Gupta, A. Mitra, M. Aslam and D. Bahadur, *RSC Adv.*, 2015, **5**, 14311–14321.
49 N. V. Jadhav, A. I. Prasad, A. Kumar, R. Mishra, S. Dhara, K. R. Babu, C. L. Prajapat, N. L. Misra, R. S. Ningthoujam, B. N. Pandey and R. K. Vatsa, *Colloids Surf., B*, 2013, **108**, 158–168.
50 Z.-Z. Fan, H.-W. He, X. Yan, R.-H. Zhao, Y.-Z. Long and X. Ning, *Polymers*, 2019, **11**, 530.
51 X. Shen, Q. Wang, W. Chen and Y. Pang, *Appl. Surf. Sci.*, 2014, **317**, 1028–1034.
52 Ç. E. Demirci, P. K. Manna, Y. Wroczynskyj, S. Aktürk and J. van Lierop, *J. Phys. D: Appl. Phys.*, 2017, **51**, 025003.
53 Q. Li, C. W. Kartikowati, S. Horie, T. Ogi, T. Iwaki and K. Okuyama, *Sci. Rep.*, 2017, **7**, 9894.
54 R. S. Joshi and P. S. A. Kumar, in *Comprehensive Inorganic Chemistry II (Second Edition)*, ed. J. Reedijk and K. Poeppelmeier, Elsevier, Amsterdam, 2013, pp. 271–316.
55 I. Apostolova and J. M. Wesselinowa, *Phys. Status Solidi B*, 2009, **246**, 1925–1930.
56 N. K. Prasad, K. Rathinasamy, D. Panda and D. Bahadur, *J. Mater. Chem.*, 2007, **17**, 5042–5051.
57 F. Arteaga-Cardona, K. Rojas-Rojas, R. Costo, M. A. Mendez-Rojas, A. Hernando and P. de la Presa, *J. Alloys Compd.*, 2016, **663**, 636–644.
58 A. Marino, A. Camponovo, A. Degl'Innocenti, M. Bartolucci, C. Tapeinos, C. Martinelli, D. D. Pasquale, F. Santoro, V. Mollo, S. Arai, M. Suzuki, Y. Harada, A. Petretto and G. Ciofani, *Nanoscale*, 2019, **11**, 21227–21248.
59 A. J. Giustini, A. A. Petryk, S. M. Cassim, J. A. Tate, I. Baker and P. J. Hoopes, *Nano LIFE*, 2010, **01**, 17–32.
60 O. Rajkovic, C. Gourmel, R. d'Arcy, R. Wong, I. Rajkovic, N. Tirelli and E. Pinteaux, *Adv. Ther.*, 2019, **2**, 1900038.
61 W. Fu, X. Zhang, L. Mei, R. Zhou, W. Yin, Q. Wang, Z. Gu and Y. Zhao, *ACS Nano*, 2020, **14**, 10001–10017.
62 L. Horev-Azaria, G. Baldi, D. Beno, D. Bonacchi, U. Golla-Schindler, J. C. Kirkpatrick, S. Kolle, R. Landsiedel, O. Maimon, P. N. Marche, J. Ponti, R. Romano, F. Rossi, D. Sommer, C. Uboldi, R. E. Unger, C. Villiers and R. Korenstein, *Part. Fibre Toxicol.*, 2013, **10**, 32.
63 S. B. Kedare and R. P. Singh, *J. Food Sci. Technol.*, 2011, **48**, 412–422.
64 N. Malhotra, J.-S. Lee, R. A. D. Liman, J. M. S. Ruallo, O. B. Villaflores, T.-R. Ger and C.-D. Hsiao, *Molecules*, 2020, **25**, 3159.
65 M. L. M. Pisciotti, E. Lima, Jr., M. V. Mansilla, V. E. Tognoli, H. E. Troiani, A. A. Pasa, T. B. Creczynski-Pasa, A. H. Silva, P. Gurman, L. Colombo, G. F. Goya, A. Lamagna and R. D. Zysler, *J. Biomed. Mater. Res., Part B*, 2014, **102**, 860–868.
66 A. A. Mieloch, M. Żurawek, M. Giersig, N. Rozwadowska and J. D. Rybka, *Sci. Rep.*, 2020, **10**, 2725.
67 P. S. Haddad, M. C. Santos, C. A. de G. Cassago, J. S. Bernardes, M. B. de Jesus and A. B. Seabra, *J. Nanopart. Res.*, 2016, **18**, 369.
68 C. Pucci, C. Martinelli, D. De Pasquale, M. Battaglini, N. di Leo, A. Degl'Innocenti, M. Belenli Gümüş, F. Drago and G. Ciofani, *ACS Appl. Mater. Interfaces*, 2022, **14**, 15927–15941.
69 C. F. Thorn, C. Oshiro, S. Marsh, T. Hernandez-Boussard, H. McLeod, T. E. Klein and R. B. Altman, *Pharmacogenet. Genomics*, 2011, **21**, 440–446.
70 K. Kupcho, J. Shultz, R. Hurst, J. Hartnett, W. Zhou, T. Machleidt, J. Grailer, T. Worzella, T. Riss, D. Lazar, J. J. Cali and A. Niles, *Apoptosis*, 2019, **24**, 184–197.

